

Effects of linear and nonlinear structural deflections on the performance and stability derivatives of high-aspect ratio wing aircraft

Martin Sohst

Thesis to obtain the Master of Science Degree in

Aerospace Engineering

Supervisors: Prof. Afzal Suleman
Prof. Christian Breitsamter

Examination Committee

Chairperson: Prof. Fernando José Parracho Lau

Supervisor: Prof. Afzal Suleman

Member of the Committee: Prof. João Manuel Gonçalves de Sousa Oliveira

November 2017

Acknowledgements

I would like to thank Professor Suleman for the opportunity to write the thesis under his supervision and his steadily support during my stay at Tecnico in Lisbon.

Likewise, I am grateful to Professor Breitsamter, who supervised my thesis at the TU Munich and made it possible for me to write my thesis externally.

For the organizational support for the stay at Tecnico, I am thankful to Professor Lau.

Special thanks go to Frederico Afonso and Jose Vale, both postdocs at Tecnico, who supported me during my working time with helpful advice and whom I can call friends now.

Further, I would like to thank the following persons, who directly or indirectly helped me with their support to finish this work: Pedro Fernandes, Éder Oliveira, Simão Rodrigues, Miguel Dias

In the end, I would like to thank my family and friends, who always supported and encouraged me during my life.

Abstract

To satisfy the demand for “greener” aircrafts, the aeronautics industry endeavours to develop more efficient aircraft. Due to higher lift-to-drag ratio, high aspect ratio wings are one of the solutions to achieve this goal. However, slender wings are more prone to higher deflections, which may lead to geometrical nonlinear behaviour. The higher deflection can lead to an earlier onset of aeroelastic instabilities such as flutter and can have a negative influence on stability behaviour.

The objective of this work is to investigate the effects of linear and nonlinear structural deflections on the flutter speed and static stability derivatives of a high aspect ratio swept wing. For the calculations low fidelity methods are used to model the aeroelastic behaviour and the prediction of the flutter speed, as well as high fidelity methods for the stability derivative calculation. A comparison was made considering different flight conditions, namely angle of attack, altitude and airspeed. In the end, a brief parametric study shows the influence of wing box thickness and its impact regarding the displacements and flutter speeds. Considering different angles of attack, steady state calculations with computational fluid dynamics were done to estimate the static stability derivatives of the rigid and the flexible wings.

The most relevant results show a slight difference in wing deformation for linear and nonlinear calculations, increasing with deflection. The nonlinear deflections are normally smaller than the linear ones, which results in higher flutter speed for the various boundary conditions. A noticeable difference in flutter speed was observed between the rigid and flexible wings due to the different vibrations modes that comprise the flutter mechanism. A decrease in wing box thickness made the wing more flexible. The resulting changes are a decrease in flutter speed and an increase of displacement. Also, an influence of the deformations could be seen on the static stability derivatives. The deformed shapes have a lower C_L and C_M , whereas the C_D/C_L is higher than for the rigid wing. A noticeable difference between the linear and nonlinear deformed wings could not be recognized.

Keywords: High aspect ratio wing, Nonlinear structural effects, Stability derivatives, Flutter speed, Aeroelastic analysis, Computational fluid dynamics

Zusammenfassung

Um der Nachfrage nach „grünen“ Flugzeugen gerecht zu werden, bemüht sich die Luftfahrtindustrie um die Entwicklung effizienterer Flugzeuge. Auf Grund des höheren Auftrieb-zu-Widerstands-Verhältnisses sind Flügel mit hoher Streckung ein Ansatz, um dieses Ziel zu erreichen. Dem gegenüber steht die höhere Anfälligkeit schlanker Flügel gegen hohe Deformationen, welche zu geometrisch nichtlinearem Verhalten führen kann. Der höhere Ausschlag kann zu früher erscheinenden aeroelastischen Instabilitäten, wie beispielsweise Flattern, führen und das Stabilitätsverhalten negativ beeinflussen.

Ziel dieser Arbeit ist die Untersuchung der Auswirkung von linearen und nichtlinearen strukturellen Deformationen auf die Flattergeschwindigkeit und Stabilitätsderivativa eines gepfeilten Flügels mit hoher Streckung. Für die Analyse kommen sowohl einfache numerische Methoden für das aeroelastische Verhalten und die Flattergeschwindigkeit, als auch umfassendere Modelle für die Berechnungen der Stabilitätsderivativa zum Einsatz. Die Ergebnisse verschiedener Flugzustände bezüglich Geschwindigkeit, Anstellwinkel und Flughöhe wurden miteinander verglichen. Die anschließende Durchführung einer parametrischen Studie zeigt den Einfluss der Flügelkastendicke auf die Deformationen und die Flattergeschwindigkeit. Schlussendlich wurden stationäre Berechnungen mit variierenden Angriffswinkeln mit den Methoden der CFD durchgeführt um statische Stabilitätsderivativa für den starren und flexiblen Flügel abzuschätzen.

Für die Verformung lässt sich ein geringer Unterschied zwischen dem linearen und nichtlinearen Modell feststellen, wobei diese Differenz mit zunehmender Gesamtverformung zunimmt. Grundsätzlich sind die nichtlinearen Verschiebungen geringer als die linearen, was zu einer höheren Flattergrenze für die unterschiedlichen Randbedingungen führt. Ein deutlicher Unterschied bezüglich der Flattergeschwindigkeiten konnte zwischen dem starren und den flexiblen Flügeln festgestellt werden. Hierbei waren die verantwortlichen Vibrationsmodi unterschiedlich für den Beginn des Flattermechanismus. Ein Verringern der Wandstärke des Flügelkastens machte den Flügel flexibler. Die resultierenden Änderungen sind eine Zunahme der Verformung und eine abnehmende Flattergeschwindigkeit. Ebenso kann ein Einfluss der Verformung des Flügels auf die statischen Stabilitätsderivativa beobachtet werden. Die verformten Flügel haben einen flacheren Verlauf bezüglich des Auftriebs- und Momentkoeffizienten. Im Vergleich mit dem starren Flügel haben sie ein höheres Widerstands-zu-Auftriebsverhältnis. Ein bemerkenswerter Unterschied zwischen den nicht linear und linear verformten Flügeln kann nicht festgestellt werden.

Schlüsselwörter: Hohe Flügelstreckung, Nichtlineare strukturelle Effekte, Stabilitätsderivativa, Flattergeschwindigkeit, Aeroelastische Analyse, CFD

Resumo

Para satisfazer a procura por aeronaves "mais ecológicas", a indústria aeronáutica tem se esforçado por desenvolver aeronaves mais eficientes. Devido a um maior coeficiente de planeio (L/D), as asas de elevado alongamento apresentam-se como uma das soluções para alcançar esse objetivo. No entanto, as asas de elevado alongamento são mais propensas a grandes deflexões, o que pode levar a um comportamento geométrico não linear. Esta maior deflexão pode levar ainda ao aparecimento de instabilidades aeroelásticas, como o flutter, mais cedo e como tal afetando negativamente a estabilidade de voo.

O objetivo deste trabalho é investigar os efeitos das deflexões estruturais lineares e não-lineares na velocidade do flutter e nas derivadas de estabilidade de uma asa de elevado alongamento com flecha. Para os cálculos são usados métodos de baixa fidelidade para modelar o comportamento aeroelástico e a previsão da velocidade de flutter, bem como métodos de alta fidelidade para o cálculo das derivadas de estabilidade. Foi feita uma comparação considerando diferentes condições de voo, nomeadamente ângulo de ataque, altitude e velocidade. No final, um estudo paramétrico breve mostra a influência da espessura do caixão da asa e seu impacto nos deslocamentos e na velocidade do flutter da asa. Considerando diferentes ângulos de ataque foram realizados cálculos estacionários utilizando mecânica de fluidos computacional para estimar as derivadas de estabilidade estática de uma asa rígida e outra flexível.

Os resultados para a asa de interesse mostram uma ligeira diferença entre as deformações lineares e não-lineares, aumentando esta com a deflexão. As deflexões não-lineares são normalmente menores que as lineares, o que resulta numa velocidade de flutter maior para as diversas condições de fronteiras. Uma diferença notável entre as asas rígida e flexível foi observada na velocidade de flutter estimada devido aos diferentes modos de vibração responsáveis pelo flutter. Uma diminuição na espessura do caixão da asa tornou a asa mais flexível. As mudanças resultantes são uma diminuição da velocidade de flutter e um deslocamento superior. Também nas derivadas de estabilidade estáticas foi notada uma variação com o aumento de flexibilidade. As formas deformadas têm um C_L e C_M mais baixos, enquanto o C_D/C_L é maior do que para a asa rígida. Não foi possível reconhecer uma diferença notável entre as deformações lineares e não-lineares da asa.

Palavras chave: Asas de elevado alongamento, Efeitos estruturais não-lineares, derivadas de estabilidade, velocidade de flutter, análise aeroelástica, mecânica de fluidos computacional

Table of content

| | |
|--|------|
| Abstract..... | II |
| Zusammenfassung | III |
| Resumo | IV |
| List of figures | VI |
| List of tables | VIII |
| List of symbols..... | IX |
| 1 Introduction | 1 |
| 2 Aeroelasticity | 4 |
| 3 Stability derivatives | 7 |
| 4 Aircraft model..... | 9 |
| 5 Computational tools and theory..... | 12 |
| 5.1 Multidisciplinary Design Optimization (MDO) Tool..... | 12 |
| 5.2 MSC Nastran | 14 |
| 5.3 MATLAB | 19 |
| 5.4 SolidWorks..... | 20 |
| 5.5 ANSYS..... | 20 |
| 6 Model validation through Eigenvalues, Eigenvectors and single load displacements | 22 |
| 7 Linear and nonlinear structural deflections and its effect on flutter speed | 24 |
| 8 Parametric study..... | 32 |
| 9 Calculation of Stability Derivatives | 38 |
| 9.1 Mesh convergence study..... | 38 |
| 9.2 Results for static stability derivatives..... | 39 |
| 10 Conclusion and future work..... | 41 |
| References | 43 |
| Appendix..... | 48 |
| A V-g and v-f graphs | 49 |

List of figures

| | |
|---|----|
| Figure 2-1: Aeroelastic Triangle of Forces with a selection of phenomena, adapted from [22]..... | 4 |
| Figure 2-2: Wing divergence as result of higher acting lift force than restoring stiffness moment..... | 5 |
| Figure 2-3: Aileron effectiveness dependent on speed, from [23] | 5 |
| Figure 2-4: Flutter as self-reinforcing oscillating effect of aerodynamic instability | 5 |
| Figure 4-1: Flight envelope according to Bombardier | 9 |
| Figure 4-2: Stick model of the aircraft in Siemens NX | 10 |
| Figure 4-3: MDOGUI model, with the aerodynamic panel model..... | 10 |
| Figure 4-4: Nastran wing model with the structural model (beam) and the aerodynamic model (panels) | 10 |
| Figure 4-5: CAD half wing-tail model in SolidWorks | 10 |
| Figure 4-6: Coordinate system used for the result presentation of the deformations, implying positive displacements bend the wing upwards. | 10 |
| Figure 5-1: Discretization of the surface into doublet elements, with the positions of the collocation point and the bound vortex, adapted from [58]..... | 15 |
| Figure 5-2: Beam spline for the structural and aerodynamic node connection | 17 |
| Figure 5-3: Wing and tail in the CFD environment and a sample of a deformed wing..... | 20 |
| Figure 7-1: Process of calculations for the displacements and the flutter speed | 24 |
| Figure 7-2: Comparison of linear and nonlinear displacement in dependency of the dynamic pressure | 25 |
| Figure 7-3: Comparison of linear and nonlinear displacement for increasing angle of attack | 26 |
| Figure 7-4: Eigenfrequencies of the first 10 modes for the rigid, linear and nonlinear wing | 27 |
| Figure 7-5: First 10 modes with corresponding frequency changes | 28 |
| Figure 7-6: Damping graph for one of the flutter analysis | 29 |
| Figure 7-7: Frequency graph for one of the flutter analysis | 30 |
| Figure 7-8: Flutter speed depending on angle of attack for the rigid, linear deformed and nonlinear deformed wing at an altitude of 0m (sea level) | 30 |
| Figure 7-9: Flutter speed for increasing altitude at an angle of attack of 5° | 31 |
| Figure 8-1: Idealized wing box with the dashed shape of the airfoil around, simplified for a rectangular wing box; with the chord c , the wing box height H , wing box width B and thickness t | 32 |
| Figure 8-2: Flutter speeds of the wing with the reduced wing box thickness; for the first in-plane mode and first torsion mode | 37 |
| Figure 8-3: Wing tip vertical displacement for the original wing and the parametric studies | 37 |
| Figure 8-4: Exaggerated representation of the gull wing deformation due to mass reduction for low angles of attack | 37 |
| Figure 9-1: Mesh convergence study results for the lift coefficient | 38 |
| Figure 9-2: Mesh convergence study results for the drag coefficient | 39 |
| Figure 9-3: Coefficients for the coefficients of lift, moment and drag | 40 |
| Figure A - 1: Rigid wing flutter graphs of the changing angles of attack at sea level..... | 49 |

Figure A - 2: Linear deformed wing flutter graphs of the changing angles of attack at sea level and the deformation data from 200 m/s.....50

Figure A - 3: Nonlinear deformed wing flutter graphs of the changing angles of attack at sea level and the deformation data from 200 m/s51

Figure A - 4: Rigid wing flutter graphs for a constant angle of attack at different Altitudes.....52

Figure A - 5: Linear deformed wing flutter graphs for a constant angle of attack at different Altitudes at the deformed state of 200 m/s.....53

Figure A - 6: Nonlinear deformed wing flutter graphs for a constant angle of attack at different Altitudes at the deformed state of 200 m/s54

List of tables

Table 6-1: Comparison of the Eigenfrequencies 22

Table 6-2: Comparison for validation of the Bombardier and the MATLAB model 23

Table 7-1: Deformation comparison at different altitudes for constant angle of attack and velocity 25

Table 7-2: Deformation comparison of different angles of attack at constant altitude and velocity 26

Table 8-1: Differences in vertical displacement for the reduced box thickness for the linear deformations 35

Table 8-2: Differences in vertical displacement for the reduced box thickness for the nonlinear deformations 35

Table 8-3: Flutter speeds for the reduced box thickness for the linear deformed wing for the first in-plane rigid body mode 36

Table 8-4: Flutter speeds for the reduced box thickness for the nonlinear deformed wing for the first in-plane rigid body mode 36

Table 8-5: Flutter speeds for the reduced box thickness for the linear deformed wing for the first torsion rigid body mode 36

Table 8-6: Flutter speeds for the reduced box thickness for the nonlinear deformed wing for the first torsion rigid body mode 36

List of symbols

| | |
|----------------------|---|
| A | Aerodynamic matrix |
| A_C | Aerodynamic damping matrix |
| A_{ij} | Aerodynamic influence coefficient matrix |
| A_K | Aerodynamic stiffness matrix |
| AR | Wing aspect ratio |
| b | Wing span |
| B | Linear strain-displacement matrix |
| B_{hh} | Modal damping matrix |
| B_{NL} | Nonlinear strain displacement matrix |
| C | Damping matrix |
| c | Wing chord |
| \bar{c} | Reference length |
| C_D | Drag coefficient |
| C_L | Lift coefficient |
| $C_{L\alpha}$ | Lift coefficient slope |
| C_M | Moment coefficient |
| $C_{M\alpha}$ | Moment coefficient slope |
| d | Nodal displacement vector |
| D | Elasticity matrix |
| D_{jv}^1, D_{jt}^2 | Real and imaginary parts of substantial differentiation matrix |
| F | Total load vector |
| F_g | Gravity load vector |
| F_t | Aerodynamic force |
| F_s | Structural force |
| f_j | Pressure on lifting element j |
| G_{ta} | Spline matrix reduced to a -set |
| G_{ts} | interpolation matrix between structural and aerodynamic grid points |
| I_{xx} | Area moment of inertia around the x-axis |
| I_{zz} | Area moment of inertia around the z-axis |
| K | Stiffness matrix |
| k | Reduced frequency |
| K_{hh} | Modal stiffness matrix |
| M | Mass matrix |
| M_{hh} | Modal mass matrix |
| N | Shape function matrix |
| n | Normal vector to the surface |
| p | Complex eigenvalue |

| | |
|---------------|--|
| P_k | Forces at aerodynamic grid points |
| q | Flight dynamic pressure |
| Q_{hh}^d | Modal aerodynamic damping matrix |
| Q_{ii} | Generalized aerodynamic matrix |
| Q_{hh}^R | Modal aerodynamic stiffness matrix |
| r | Distance between a point and the source or doublet location |
| S | Surface area |
| S_B | Surface boundary |
| S_{kj} | integration matrix |
| u | displacement vector |
| U | Potential energy |
| u_g | Displacements at structural grid points |
| u_h | modal amplitude vector |
| u_s | Displacements at structural grid |
| u_t | Displacements at aerodynamic grid points |
| u_x | Displacement in chord direction |
| u_z | Displacement in out-of-wing-plane direction |
| $u_z/(b/2)$ | Dimensionless vertical tip displacement |
| V | Velocity |
| w_j | Downwash |
| w_j^g | Static aerodynamic downwash |
| $WTFAC$ | Matrix of empirical correction factors |
| x | System degrees of freedom displacement vector |
| \dot{x} | System degrees of freedom velocity vector |
| \ddot{x} | System degrees of freedom acceleration vector |
| \bar{x} | System degrees of freedom amplitude vector |
| α | Angle of attack |
| γ | Transient decay rate coefficient |
| δ_s | Source strength in Dirichlet boundary condition |
| δ | virtual work displacement |
| ε | Strain vector |
| Λ | Sweep angle |
| μ | Doublet strength |
| μ_l | Doublet strength at the lower surface of the trailing edge |
| μ_u | Doublet strength at the upper surface of the trailing edge |
| ρ | Air density |
| σ | Stress vector |
| Φ | Potential |
| Φ_∞ | Free-stream potential |
| Φ_{ai} | Matrix of i-set normal mode vectors in the physical a -set |

ω Natural frequency

1 Introduction

Motivation

Travel and transportation by aircraft is still an increasing market and will also be in the nearer future according to forecasts [1, 2]. Besides the demand for noise pollution reduction (especially near airports), as well as the use of sustainable energy sources, the call for “greener”, more fuel-efficient aircraft has grown in the last decades. That forced the original equipment manufacturers to develop new solutions for existing aircraft and focus on researching novel designs to fulfil those requirements.

One of the main goals is therefore to reduce the drag in an aircraft. There were already a lot of improvements in the last years to reduce the fuel consumption and the environmental impact by developing more efficient engines, the more intensive use of lightweight material and structural optimizations. Although, it is seen that for the conventional aircraft configuration a saturation is reached where it is difficult to improve it further [3]. New approaches for a reduction in drag and therefore an increase in efficiency are manifold. Unconventional designs such as out-of-plane configurations like the joined wing [4], strut-braced wing [5], X-wing or box wing [6] provide approaches for improvement. Novel concepts, namely blended wing bodies (BWB) [7], high aspect ratio wings [3], morphing structures [8], boundary layer control and adaptive wings [9] offer likewise possible solutions.

Background

The object of investigation in this work was an early stage high aspect ratio wing configuration, which was provided externally. The benefit of a high aspect ratio wing is the reduced induced drag which leads to a better performance, namely a higher lift-to-drag ratio and longer ranges due to higher efficiency [10] as well as lower chord wise airflow separation distances [3]. However, this design faces some drawbacks as well. This is the reason why the introduction in the commercial sector has been delayed. For large aircraft, there is a limit in span as described in the size characterization of the FAA [11] to operate on airports. This is the reason why often the less effective, but space saving wingtip elements are used. The slender wing has to resist a higher root bending moment compared to a conventional wing with the same area and is more prone to higher deformations. This higher structural flexibility can cause displacements where the behaviour is no longer linear, in fact nonlinear effects start appearing. Those non-linearities include geometrical non-linearities, where the initial geometry of the structure changes significantly. This means in particular, that the effective span of the wing decreases compared to the initial condition. Hence, less lift is produced which influences the forces and thereby a different displacement results. Consequently, high deformations may change the natural frequencies and mode shapes, which influences the aeroelastic reactions of several flight conditions. Therefore, boundaries of earlier occurring aeroelastic phenomena such as divergence, buffeting or flutter must be known and investigated to ensure a safe flight in all conditions. Another source for non-linearities is damping, when the forces contribute to non-linear responses. Also, material behaviour can be a reason, when the strain-stress relation is not linear anymore. As the designs of interest should also be able to operate in a high-speed regime (transonic), highly elastic structures must be developed with special caution regarding this sensitive topic.

Another important feature of high aspect ratio wings is the influence of contingent nonlinear deformations on stability and control behaviour of an aircraft [12]. The aircraft stability characteristics are divided into static stability and dynamic stability. The former is understood as the steady reaction of the aircraft in a nonvarying airflow whereas the latter is the reaction of a disturbance or a changing environment. To know the behaviour of an aircraft, it is important to know the derivatives to ensure flight stability in an early design phase. Traditionally, the determination of stability takes place after wind tunnel testing [13]. This has some drawbacks, namely the high expenses in the preliminary design stage, the cost of model changings and the testing [14]. An even more accurate method of estimation is a flight test with a full-scale aircraft. But in a preliminary design stage, this is not feasible. In the last decades, the method of computational fluid dynamics (CFD) was more and more accepted in the development process of new aircraft, as it is cost efficient and optimization is more efficient to handle [15]. Nevertheless, it is still time consuming, depending on the accuracy and the investigation of fast and reliable methods is an ongoing process. Several different approaches for calculation, especially of dynamic stability derivatives, were published in the last decade [15, 16, 17].

The pre-existing model for the examination is a stick model of the aircraft from which the data was extracted to analyse the wing only, with the purpose of reducing computational cost and keeping the design level on a comprehensible stage. As there was no further data provided, airfoil data was used from a former project with a similar wing.

For the present work, a multidisciplinary design tool was used to model the wing and calculate the linear and nonlinear deformations at specific flight conditions. To model the structure, an equivalent beam model was used; the aerodynamic model is based on the panel method where a simplified flow field is assumed (inviscid, irrotational and incompressible). The influence of each to the other one is done by a fluid structure interaction (FSI) model. First, a model transfer was done and validation were then executed with different single static loads to verify the correct data input. After that, a comparison between the linear and nonlinear structural deflection was done. With the generated data, a Nastran model was built with the help of a MATLAB script and within Nastran an analysis took place to investigate the occurrence of aeroelastic issues within the flight envelope, namely flutter, for the structural deflections and to outline possible differences in the behaviour (flutter boundaries).

For the static stability derivatives, the traditional and well reported method of linear interpolation was used [15, 18, 19]. For different angles of attack α and the corresponding deformed wing, the moment coefficient C_M in a steady state simulation was calculated and the slope of the pitching moment $C_{M\alpha} = \Delta C_M / \Delta \alpha$ was interpolated. This also can be done by finite differences, automatic differentiation or adjoint methods [18], but due to the simplicity of the first method, it was the preferred one. Following a comparison between the $C_{M\alpha}$ of the rigid, the linear deformed and the nonlinear deformed wing took place.

The calculation of the dynamic stability derivatives is more sophisticated and different approaches were investigated by researchers [15, 18, 20]. Still, there is not a flawless and always useable method and always one has to be adapted to a specific problem. Due to the restricted schedule for the work, an estimation of the dynamic stability derivatives was beyond the scope.

Due to challenging time aims and higher computational cost with increasing speeds, the investigation for the aircraft of interest was carried out in a lower flight regime than transonic.

Objectives

The main purpose of this work is the investigation of the properties of a preliminary designed high aspect ratio wing. For that, the influence of linear and nonlinear structural deflections is examined and compared with each other as well as with a rigid wing. Besides the displacement of the wing, the flutter boundary is taken as tool of comparison. To get an idea of the flight stability, a short introduction into stability derivatives is given.

Thesis Layout

The structure of the thesis hereby is as followed:

- Chapter 2: Insight into aeroelasticity and the occurring phenomena as well as a short historical overview of the experience and development within the last hundred years.
- Chapter 3: Synopsis of stability and stability derivatives, with the background of the traditional estimation and calculation methods for the static and dynamic stability derivatives.
- Chapter 4: The preliminary aircraft model is introduced and the different models used in this work are shortly described.
- Chapter 5: An overview of the computational tools and their background is given in this chapter.
- Chapter 6: The model created with the framework is validated against the original model under different aspects. A simple comparison of eigenfrequencies and mode shapes takes place as well as displacement comparisons caused by single point loads.
- Chapter 7: Presentation of the results for the linear and nonlinear deformations of the wing and a comparison between the two. Also, the influence of the displacements on the flutter boundary is discussed.
- Chapter 8: A parametric study takes place to investigate the influence of a structural change – with the purpose of mass reducing – to the displacements and the flutter boundary.
- Chapter 9: In this chapter, the calculation of the static stability derivatives is described and the results are discussed.
- Chapter 10: Finally, the results are recapitulated and an outlook for possible future work is presented

2 Aeroelasticity

In general, aeroelasticity can be separated into two occurring types, static and dynamic aeroelasticity [21]. The former describes the interaction between aerodynamic and elastic forces and the mutual influence as a wing is not perfectly rigid. An aerodynamic force leads to a structural shape change, which again leads to a change in the aerodynamic forces and so on. This can lead either to an equilibrium state where those forces balance out or to a critical structural failure if the maximum stress exceeds the capability of the material. Examples of this type of issues are divergence and control reversal. In dynamic behaviour, the inertia forces are also considered in the interaction with aerodynamic and elastic forces. Induced oscillations due to gust, with frequencies similar to the natural frequencies of the structure, can lead to a failure of the structure. Other phenomena for dynamic aeroelasticity include flutter and buffeting.

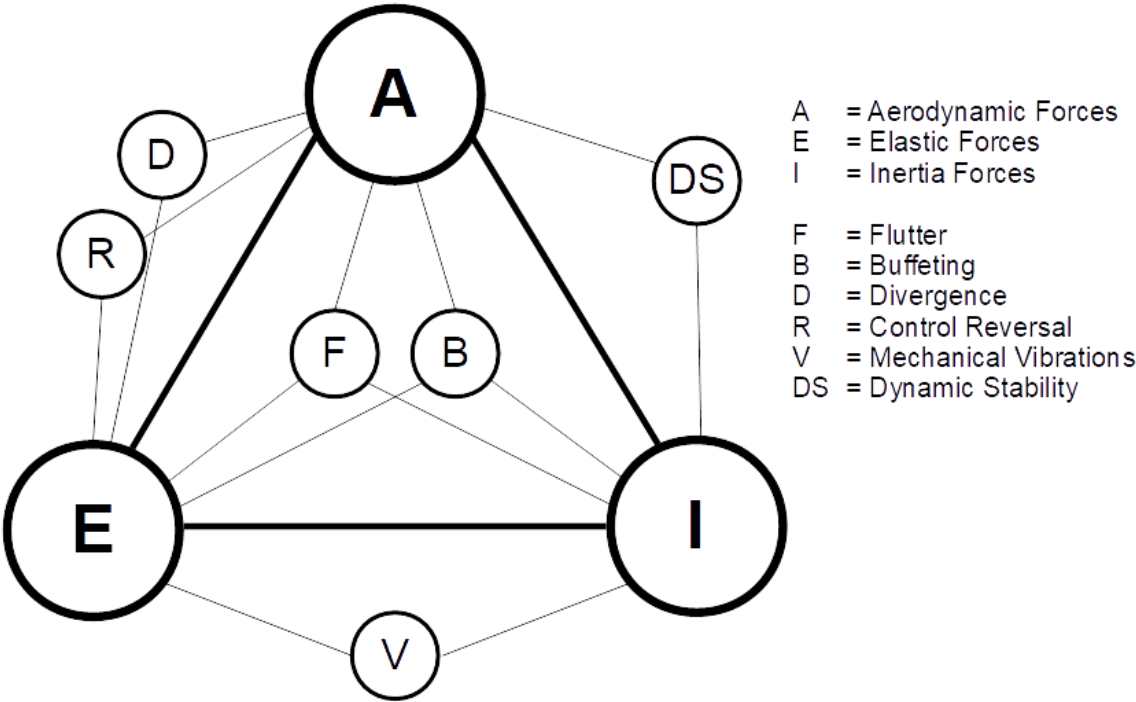


Figure 2-1: Aeroelastic Triangle of Forces with a selection of phenomena, adapted from [22]

Figure 2-1 shows different phenomena of aeroelastic behaviours and where they can be found according to their appearance. Hence, all different kinds of aeroelastic phenomena can be placed at the corresponding spot in the triangle. Typical and well-known problems appearing on different positions are, for example, divergence, control reversal, buffeting and flutter.

Divergence is a static aeroelastic phenomenon that appears at a specific speed (divergence speed). The aerodynamic forces, acting on the aerodynamic centre of the wing in front of the elastic axis, lead to a torsional deflection. At the divergence speed, the moment due to the lift exceeds the restoring elastic moment and can cause a failure (see Figure 2-2). The wing, therefore, becomes statically unstable. Parameters affecting the divergence speed are the torsional stiffness of the wing and the distance

between the elastic axis and the aerodynamic centre. In their investigation, Diederich and Budiansky [23] came to the result, that moderate or high swept back wings cannot diverge, as the incidence angle due to the aerodynamic forces opposes the lift.

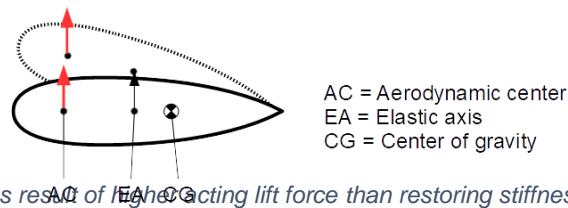


Figure 2-2: Wing divergence as result of lift force acting lift force than restoring stiffness moment

Control reversal occurs when a deflection of a control surface, such as aileron or elevator, has the opposite reaction to the one intended. With an increasing velocity, the effectiveness of a constant deflection changes, and at one point it even occurs a contrary reaction, where the elastic reaction of the structure nullified or exceed the intended effects (see Figure 2-3). Picturing the effect of aileron control reversal, a lowered aileron increases the lift on one side, but leads to a moment around the elastic axis reducing the angle of attack. With increasing speed, this reacting moment increases too and generates the reversal effect.

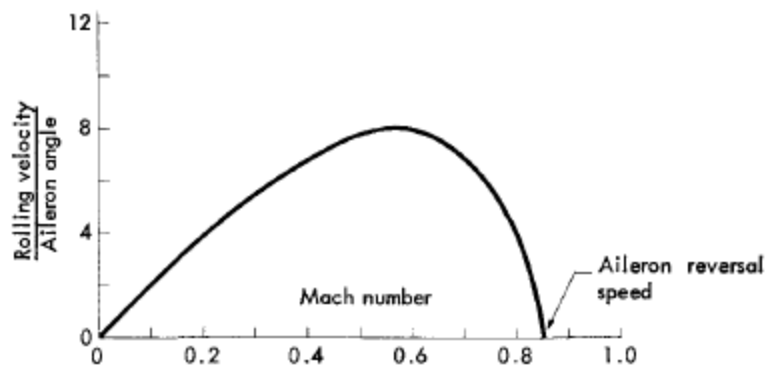


Figure 2-3: Aileron effectiveness dependent on speed, from [23]

Buffeting is the reaction of the aircraft structure behind parts where poor airflows appeared. This can cause vibrations with a frequency near the structural eigenfrequencies. A clean airflow over the wings helps to counteract this phenomenon.

Flutter often, but not exclusively, emerges if two eigenfrequencies of a structure couple (normally a torsion mode with a bending mode) due to the increasing flow speed and the structural damping of one of the mode shapes becomes positive (see Figure 2-4). This inevitably leads to a structural failure and is one if not the most critical issue that has to be handled within aircraft development [22].

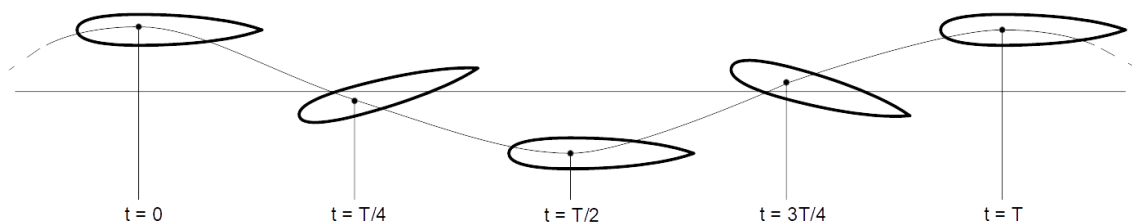


Figure 2-4: Flutter as self-reinforcing oscillating effect of aerodynamic instability

Flutter is a dynamic instability of an elastic body, meaning that on a perfectly rigid body, it would not occur. Caused on bodies with high aerodynamic loads, for instance wings, tail and control surfaces, it extracts energy from the surrounding airflow, leading to self-excited oscillations (see Figure 2-4). Above a specific speed U_F , the response to a disturbance, like a gust or a high-g manoeuvre, cannot be damped anymore and the structure exhibits a sustained harmonic oscillation. This flutter boundary is marked by the coupling of two rigid body modes. The investigation of flutter within a system is done by studying the stability of infinitesimal motions.

In the first years of flight, the speed of aircraft was low and first serious problems of aeroelasticity did not occur until World War 2. The structure of planes was rigid enough to suppress any possible phenomena. An early description of aeroelastic failure was presented by Griffith Brewer for the incidence of professor Samuel P. Langley (Smithsonian Institute) [22]. He described the phenomenon as we describe today torsional divergence. This could be one of the reasons why biplanes became more common, especially for fighters with higher performance, as they provide a higher torsional wing stiffness [22]. The commonly occurring problem during that time was tail flutter. The solution with a structural stiff tail is used ever since then. Two infamous examples are: the Handley Page 0/400 bomber, which had two low-frequency vibration modes for the fuselage and tail; and the DH-9 which causes a lot of losses in operation. It then appeared again when the engineers switched back from biplanes to monoplanes, as the torsional stiffness, which was designed with biplane rules, was too low. A first flutter test was introduced by Von Schlippe in Germany in 1935 [24], where he vibrated the aircraft structure with progressively higher speeds and took their amplitude as a function of speed. With an occurring infinite amplitude (because of zero damping) he assumed flutter. Around that time, mathematical formulations of the problem of flutter were developed, for example Frazier and Duncan [25] or Theodorsen [26]. In the following decades, more possibilities for the calculation of flutter came up and are nowadays established in the aircraft development.

In the last years, the field of research in nonlinear aeroelastic behaviour, where the structure exceeds linear deformations, increased [27]. This concerns especially wings with a high aspect ratio and a lightweight structure, where high deformations can be found.

3 Stability derivatives

To characterize the ability of the aircraft to react to a disturbance and its behaviour, stability derivatives are used [12, 28, 29].

Those are based on the linearized equations of motion of the aircraft and are derived from small disturbance theory and rigid body dynamics [30]. They are usually separated into longitudinal, Equation (3-1), and lateral motions, Equation (3-2). Taken from Nelson [31] are the following equations of motion:

$$\begin{bmatrix} X_u & X_w & 0 & -g \\ Z_u & Z_w & u_0 & 0 \\ M_u + M_{\dot{w}}Z_u & M_w + M_{\dot{w}}Z_w & M_q + M_{\dot{w}}u_0 & 0 \\ 0 & 0 & 1 & 0 \end{bmatrix} \cdot \begin{bmatrix} \Delta u \\ \Delta w \\ \Delta q \\ \Delta \theta \end{bmatrix} + \begin{bmatrix} X_\delta & \\ Z_\delta & \\ M_\delta + M_{\dot{w}}Z_\delta & \\ 0 & \end{bmatrix} \cdot [\Delta \delta] = \begin{bmatrix} \Delta \dot{u} \\ \Delta \dot{w} \\ \Delta \dot{q} \\ \Delta \dot{\theta} \end{bmatrix} \quad (3-1)$$

$$\begin{bmatrix} Y_\beta & Y_p & Y_r & -1 & \frac{g \cdot \cos \theta_0}{u_0} \\ u_0 & u_0 & u_0 & 0 & u_0 \\ L_\beta & L_p & L_r & 0 & 0 \\ N_\beta & N_p & N_r & 0 & 0 \\ 0 & 1 & 0 & 0 & 0 \end{bmatrix} \cdot \begin{bmatrix} \Delta \beta \\ \Delta p \\ \Delta r \\ \Delta \phi \end{bmatrix} + \begin{bmatrix} 0 & Y_{\delta r} \\ L_{\delta \alpha} & L_{\delta r} \\ N_{\delta \alpha} & N_{\delta r} \\ 0 & 0 \end{bmatrix} \cdot [\Delta \delta] = \begin{bmatrix} \Delta \dot{\beta} \\ \Delta \dot{p} \\ \Delta \dot{r} \\ \Delta \dot{\phi} \end{bmatrix} \quad (3-2)$$

With an indicial approach, forces and moments can be expressed as superposition of steps with varying amplitude [30]. For instance, the pitch moment can be written as:

$$C_m = C_{m_0} + C_{m_\alpha} \Delta \alpha + C_{m_{\dot{\alpha}}} \Delta \dot{\alpha} + C_{m_q} q + C_{m_{\dot{q}}} \dot{q} + \hat{\Delta}(\Delta \alpha, q). \quad (3-3)$$

The stability derivatives in the formulation above are the partial derivatives. For the static derivatives, the time-based terms can be neglected, and a steady calculation can take place. This leads to the formulation for C_{m_α} as:

$$C_{m_\alpha} = \frac{\partial C_m}{\partial \alpha} = \frac{\Delta C_m}{\Delta \alpha}, \quad (3-4)$$

where with two steady simulations the value of C_{m_α} can be estimated. It gets more accurate, if the two calculation points are close together, but requires then a high resolution for a wide range.

The first mention was by Bryan [32] in 1911, who introduced the concept of using stability of aerodynamic derivatives. There is a distinction between static and dynamic stability derivatives, and some sources also separate additionally the control derivatives [33]. The former one describes the quality of the aircraft to return to a balanced state after an initial disturbance. The dynamic derivatives display the ability to recover the vehicle with dynamic damping moments related to time response [15]. Hence, it is of utmost importance, to know the behaviour of the aircraft for the quality of flight.

Traditionally, wind tunnel testing was used to estimate the derivatives. This has some drawbacks: the high costs for models, especially for the preliminary design, as there are a lot of design points not known yet; also, the limited representation of the flight conditions, where only scaled models can be used and for example Reynolds numbers differ; a further problem is the influence of the support in the wind tunnel, as it might negatively affect the determination. The most accurate extraction of the derivatives could be

achieved by flight testing, but the exceedingly high costs restrict this method as well as the availability of full scale aircrafts at early design stages. With the emerged methods of computational fluid dynamics (CFD), it is possible to model the aircraft accurately, even in an early design stage and estimate the stability derivatives. Even though, this method can be of high computational cost, too. Especially the determination of the dynamic stability derivatives can be very complicated.

For the static derivatives, a steady flow calculation can be carried out and with the help of finite differences, automatic differentiation, adjoint methods or interpolation between two solutions, the static stability derivatives can be estimated [15, 18, 19]. In this work, the simplest method was chosen, calculating different steady states and interpolating the static derivatives between the results. The reason for this choice was the simplicity and reliability. The drawback of this approach is the high resolution needed regarding different angles of attack to depict the curve with enough accuracy. But as it should be mainly a comparison between the rigid and the deflected wings, it was taken even with a lower resolution.

For the dynamic stability derivatives, there will be given just a short overview, as it could not be dealt in more detail due to the restricted time. In general, it is more complex to estimate those derivatives, as they are time dependent and can usually not be calculated with steady state solutions.

Babcock and Arena [34] approached the problem with a non-inertial reference frame, which they used to decouple velocity and position. They reported a reduction in computational time whereby they could maintain the accuracy as if the calculation of velocity and position would be excited simultaneously. Limache and Cliff [35] also used a non-inertial reference frame, combined with a steady state solution. With their method, they could estimate multiple rotary dynamic derivatives, but it is sophisticated to apply this in general. Park and Green [36] used a rotating non-inertial reference frame likewise, applying automatic differentiation to obtain single dynamic derivatives with a single solution. Although it shows to be fast, not all derivatives could be computed.

Another possibility to obtain the dynamic derivatives is a derivation of the wind tunnel testing, adapted for CFD. To get the derivatives, the computational model is undergoing a harmonically forced oscillation, where the resulting forces and moments are used for calculating the dynamic derivatives. In this connection, the aerodynamic forces and moments are assumed as dependent on instantaneous values of disturbance velocities, control angles and their rates, and can be obtained by a Taylor series expansion while high order terms are neglected [17]. This was done, for example, by DaRonch *et al.* [17, 20] with the Standard Dynamic Model and the Transonic Cruiser as well as by Murman [19] with a reduced frequency approach with the Basic Finner Missile and the Standard Dynamic Model. Mialon *et al.* [16] did wind tunnel tests as well as computational simulations to compare small and large amplitude oscillations.

Further Ghoreyshi *et al.* [37] proposed the use of reduced order models (ROM) together with a step function and their response within Reynolds-averaged Navier-Stokes (RANS) simulations. Mi *et al.* [15] proposed a step response calculation to determine the static and single dynamic stability derivatives. However, the method was just introduced and further validation must be carried out as stated by the authors.

4 Aircraft model

The aircraft of interest is a regional jet with an empty weight of 38000 lb, a maximum take-off weight of around 52000lb and a fuselage length of 28m. The wing is assembled as a low wing configuration with a wingspan of 26m, an aspect ratio of 12, a leading edge sweep of 28 degree and winglets. The dihedral is 2.8° in the inner wing section and 2.1° in the outer section, respectively. The engine nacelles are mounted on the aft fuselage and the horizontal stabiliser is executed as a T-tail. The landing gear was already considered in this preliminary design. The estimated cruise speed is Mach 0.76 and the dive speed is Mach 0.82, both for flight altitudes between 30000 ft. and 41000 ft.

The flight envelope is seen in the diagram below (Figure 4-1).

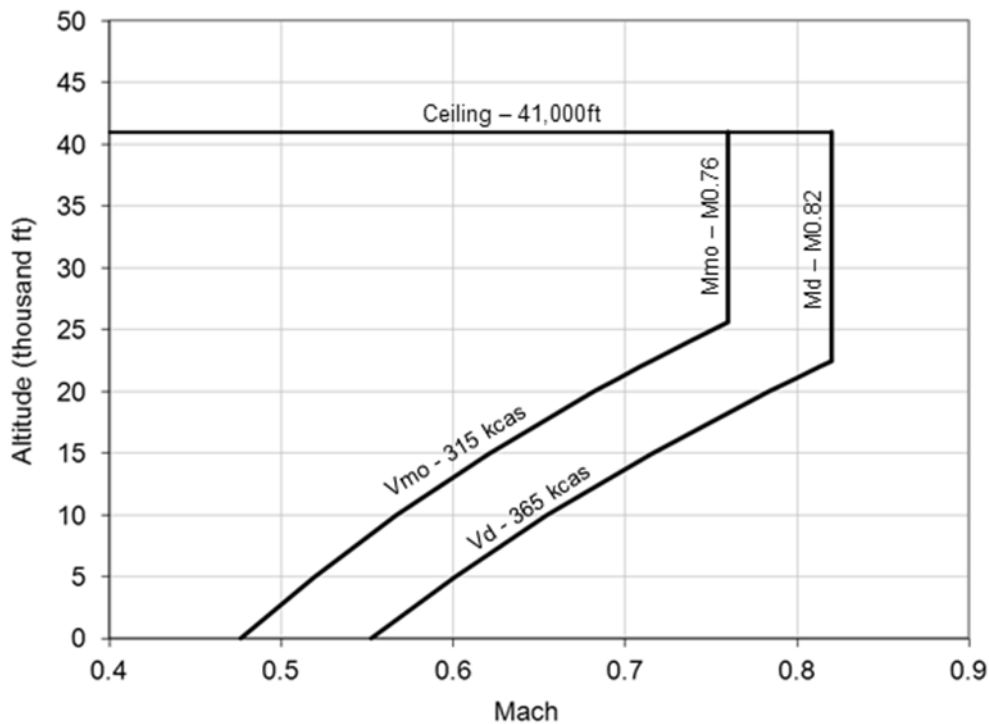


Figure 4-1: Flight envelope according to Bombardier

The provided data was given as a stick model as seen in Figure 4-2, out of which structural properties were extracted. Those included the position of structural nodes (wing shape and reduced beam), area moments of inertia, beam/wing box area, mass moment of inertia, mass and mass position. A model for the fluid-structure-interaction (FSI) was then induced, consisting of an equivalent beam for the structure and a panel model for the aerodynamics. Since no specific airfoil data was available, the airfoils from a former project of a similar transonic regional aircraft of comparable size were considered, despite the lower aspect ratio (9). The Nastran model for flutter calculation was a beam model too for the structure and the doublet lattice method (DLM) was used for the aerodynamics. For the deformed wing (either linear or non-linear deformed) the vertical displacement was considered for creating the Nastran model for the structural and the aerodynamic models. Opposing to that, in the DLM model the cambered airfoil as well as the internal twist along the wing were not considered in the calculations. A CAD model was derived from the data for preparing the CFD calculations. (Figure 4-5). As no surface data was given,

the transition from the wing to the winglet had to be modelled by hand. In the development process in the industry, this usually is a problem of optimization to achieve a smooth transition with low drag. In this work was only considered to have smooth edges. Correspondingly, the solution is not assumed as optimal.

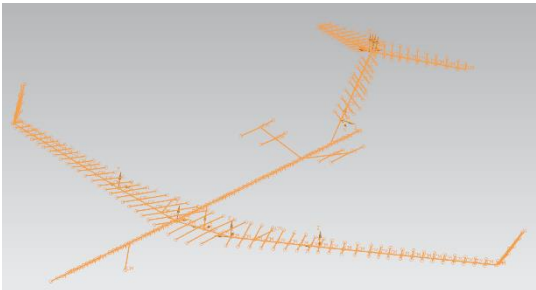


Figure 4-2: Stick model of the aircraft in Siemens NX

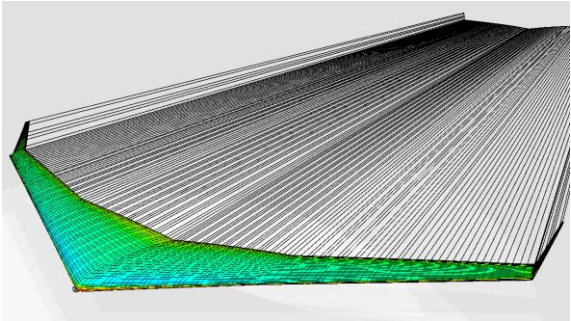


Figure 4-3: MDOGUI model, with the aerodynamic panel model

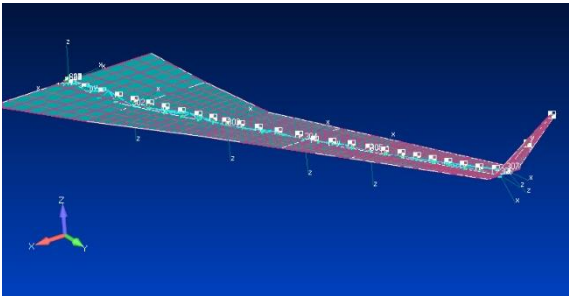


Figure 4-4: Nastran wing model with the structural model (beam) and the aerodynamic model (panels)

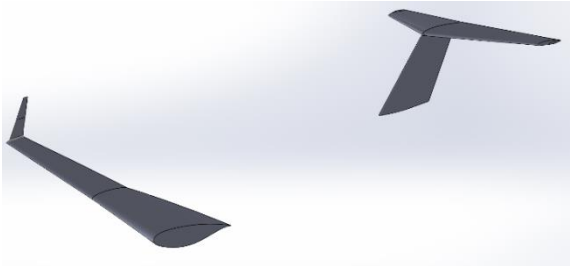


Figure 4-5: CAD half wing-tail model in SolidWorks

Since different tools were used and some of them have a stated coordinate system (Nastran and MDOGUI), a coordinate transformation was necessary between the different models. Therefore, the results also were received in different base coordinate systems. However, for the result discussion and presentation, a uniform base coordinate system was used. Here, the x-axis is along the chord line of the wing, with the positive direction in flight direction. The z-axis is in lift direction, with its positive direction in the resulting lift force direction (upwards). The y-axis completes the coordinate system with running along the wing. A schematic representation is illustrated in Figure 4-6.

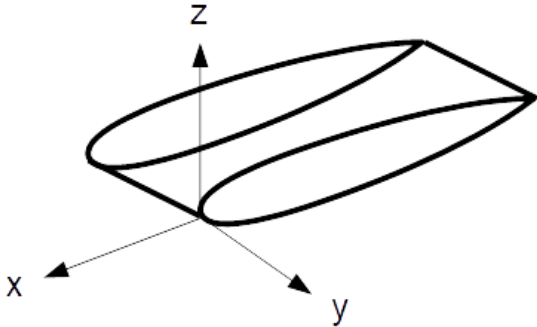


Figure 4-6: Coordinate system used for the result presentation of the deformations, implying positive displacements bend the wing upwards.

For a faster investigation, the aircraft model was reduced only to the wing for the deformation and flutter investigation and consisted of a wing-tail configuration with a rigid tail and constant distance between wing root tip and tail root tip for the static stability derivatives calculation. Also, due to symmetry, the CFD calculations were performed with just half of the model. This could be done especially as it were only calculated longitudinal static stability derivatives. Those simplifications aimed for a reduced computational cost.

The novelty of this aircraft is the combination of a high aspect ratio wing with a high speed in the transonic region. This can cause changes in aerodynamic and structural behaviour and consequently the aeroelastic behaviour shall be investigated. However, the transonic condition could not be depicted within the low fidelity models properly.

5 Computational tools and theory

In this chapter, an overview of the used programs as well as the corresponding theory for solving is given. In the first part of the flight characteristic investigation, the flutter speed was estimated to ensure that the wing could be operated in the desired speed region. For that, the programs used were: a multidisciplinary design optimization tool (MDOGUI) for the aeroelastic deformation of the wing; Nastran for the flutter determination; and MATLAB as a helping tool. For the second part, the determination of stability derivatives, the wing was modelled in Solid Works and analysed in Ansys CFX.

5.1 Multidisciplinary Design Optimization (MDO) Tool

With this tool, the linear and nonlinear deflections of the aircraft for the different flight states were calculated. The framework is established as a preliminary design tool for aircraft and its aeroelastic module is explained in more detail in [38] and [39]. It has the capability of modelling an aerodynamic model, structural model, fluid-structure-interaction (FSI), engines, payload and acoustics so far. Used in this work are the aerodynamic, structural and FSI parts.

The aerodynamic model is based on potential flow formulation, as it is designed for preliminary design of aircraft and has to be fast. It uses a three-dimensional panel method to do so. The flow is assumed as incompressible, inviscid and irrotational. With the Prandtl-Glauert correction for compressibility it is usable in a low Mach regime up to Ma 0.65, if viscous effects are low (e.g. boundary layer separation).

With those assumptions, for the velocity potential $\Phi(x, y, z)$ the following formulation can be written with the Laplace's equation:

$$\nabla^2 \Phi = 0. \quad (5-1)$$

For the steady case, two boundary conditions are required

- impermeability condition (no normal velocity on the body surface), $\nabla \Phi \cdot \mathbf{n} = 0$,
- far field condition (disappearing motion far from the surface), $\lim_{r \rightarrow \infty} (\nabla \Phi - \mathbf{v}) = 0$.

The equation is solved by applying Green's Theorem [40] which then leads to the formulation:

$$\Phi(x, y, z) = -\frac{1}{4\pi} \int_{S_B} \left[\delta \left(\frac{1}{r} \right) - \mu \mathbf{n} \cdot \nabla \left(\frac{1}{r} \right) \right] dS + \Phi_\infty, \quad (5-2)$$

with δ and μ are the source and doublet strength, respectively, r is the distance between the point (x, y, z) and the source/doublet position, \mathbf{n} is the normal vector to the surface, S_B the surface boundary and Φ_∞ the free-stream potential.

Regarding the boundary conditions, the far field is respected and a Dirichlet boundary condition is used by the developers to fulfil the impenetrability condition on the surface, where the potential enclosed by the surface is $\Phi = \Phi_\infty$. The formula (5-2) can be expressed as [40]:

$$\frac{1}{4\pi} \int_{body+wake} \mu \frac{\partial}{\partial n} \left(\frac{1}{r} \right) dS - \frac{1}{4\pi} \int_{body} \delta_s \left(\frac{1}{r} \right) dS = 0. \quad (5-3)$$

The source strength for solid bodies is formulated as follows:

$$\delta = -n \cdot \nabla \Phi_{\infty}. \quad (5-4)$$

To achieve a solution the model of the wake is implemented with the Kutta condition as constant doublet distribution:

$$\mu = \mu_u - \mu_l, \quad (5-5)$$

with μ_u and μ_l being doublet strengths at the upper and lower surface of the trailing edge, where the wake extends.

By integration of the integrals of formula (5-3) for each surface panel, the so called aerodynamic influence coefficients can be obtained and the problem can be solved. Differentiating leads to the tangential velocity for each panel and with the Bernoulli's potential flow equation, the pressure can be computed.

For higher subsonic flows, a pressure correction is implemented, namely Prandtl-Glauert. To get information in more detail about the implementation of the aerodynamic model, it is referenced to the associated literature [38, 39].

The structure of the wing is modelled as a flexible beam, as it catches the most important properties. It is based on the finite element method (FEM) and the Euler-Bernoulli beam theory, which consists of 2 nodes with 6 degrees of freedom (DOF) each, which comprises one bar, two beams and one torsion, in a sum of 4 decoupled elements. With the shape function $[N]$ and the nodal displacements $\{d\}$ the displacement field $\{u\}$ can be described as:

$$\{u\} = [N]\{d\}. \quad (5-6)$$

Whereas the strain field $\{\epsilon\}$ is formulated with the strain-displacement matrix $[B]$ and the nodal displacements:

$$\{\epsilon\} = [B]\{d\}. \quad (5-7)$$

The stress field $\{\sigma\}$, as with an isotropic and elastic material, can be written with the elasticity matrix $[D]$ as:

$$\{\sigma\} = [D]\{\epsilon\}. \quad (5-8)$$

With the potential energy U of a single element with the stiffness matrix $[K]$ and the load $[F]$ being calculated as follows:

$$U = \frac{1}{2}\{d\}^T[K]\{d\} - \{d\}^T\{F\}. \quad (5-9)$$

Here, the load vector $[F]$ includes, besides the external loads, also the self-weight of the wing, where the gravity load F_g is obtained by the product of gravity acceleration $\{g\}$ and mass matrix $[M]$:

$$[F_g] = [M]\{g\}. \quad (5-10)$$

The static equilibrium equation can then be expressed as:

$$\frac{\partial U}{\partial \{d\}} = 0 \leftrightarrow [K]\{d\} = \{F\}, \quad (5-11)$$

presuming a steady state of the potential energy regarding the nodal displacement.

The considerations of nonlinearities to the geometry alters the strain field $\{\epsilon\}$, while the displacement field is maintained. Correspondingly, the strain is divided into linear and nonlinear components:

$$\{\epsilon\} = ([B_L] + [B_{NL}])\{d\}, \quad (5-12)$$

with the linear and nonlinear displacement matrixes, $[B_L]$ and $[B_{NL}]$, respectively. As the equilibrium equation is of nonlinear form, a numerical iterative method is used to solve it. Implemented for this purpose is the Newton-Raphson method. More detailed information can be gathered from the referring literature for the tool [38, 39], and the method [41].

To calculate the aeroelastic behaviour, a coupling between the aerodynamic and the structural model is required. For that, a fluid-structure-interaction (FSI) model was implemented. It is monolithic, as the solution advances with the convergence between the structural and aerodynamic model. It is as well loosely-coupled, as the structural and aerodynamic models are computed independently and brought together with the FSI algorithm [38]. Therefore, the loads from the aerodynamic are passed to the structure, as well as the displacements are transferred the other way around. The steady aeroelastic expression calculated in the structural model assumes the form:

$$[K]\{x\} = [M]\{g\} + [A_K]\{x\}, \quad (5-13)$$

where $\{x\}$ are the DOFs of the system and $[A_K]$ is the aerodynamic stiffness.

5.2 MSC Nastran

This program was used to calculate the flutter speeds for different flight conditions. The input file, consisting of a header (parameter declaration) and bulk data was automated written using a MATLAB script with the data from the MDO output. Following, the theoretical background will be described.

Theoretical background

Same as in the MDO tool, three different sub models are necessary for an aeroelastic analysis. First the structural model, which is composed of beam elements. For the aerodynamic model, which is presented by surfaces, using the Doublet lattice method (DLM). And finally, splines must be used to connect the structural and aerodynamic model. For the theory, mainly the Nastran documentation was consulted as there is described how the program calculates the solution for the different problems [42].

The structural model consists of beam elements which are aligned in the elastic axis of each cross-section of the wing. The start and end points of each beam are given by grid points in each cross-

section. Further, the model contains the material properties, inertia moments and the boundary conditions. The whole mass of the wing is added by mass points, located regarding the given data from the provider, rather than by area and density. Therefore, the mass of a cross-section part is concentrated in those points and the mass of the beams themselves is set to zero (zero density).

Out of the six implemented theories for aerodynamic calculation in Nastran, the one used was the DLM for subsonic lifting surfaces, as it is recommended in the Nastran documentation [42] It is an extension of the steady Vortex-Lattice method to unsteady flow and is therefore based on linearized aerodynamic potential theory [43], with an undisturbed flow, which is uniform and can be either steady or with a harmonic gust. The lifting surfaces (panels) are aligned nearly parallel to the flow.

The panels themselves are divided into small trapezoidal boxes. Their edges are aligned parallel to the flow direction of the free stream and the fold and hinge lines are on their boundaries. For a reference or control point, one is taken laying span wise in the middle of the box and on the three-quarter chord line (see Figure 5-1). The lifting pressure is defined on a line at the one-quarter chord of the box.

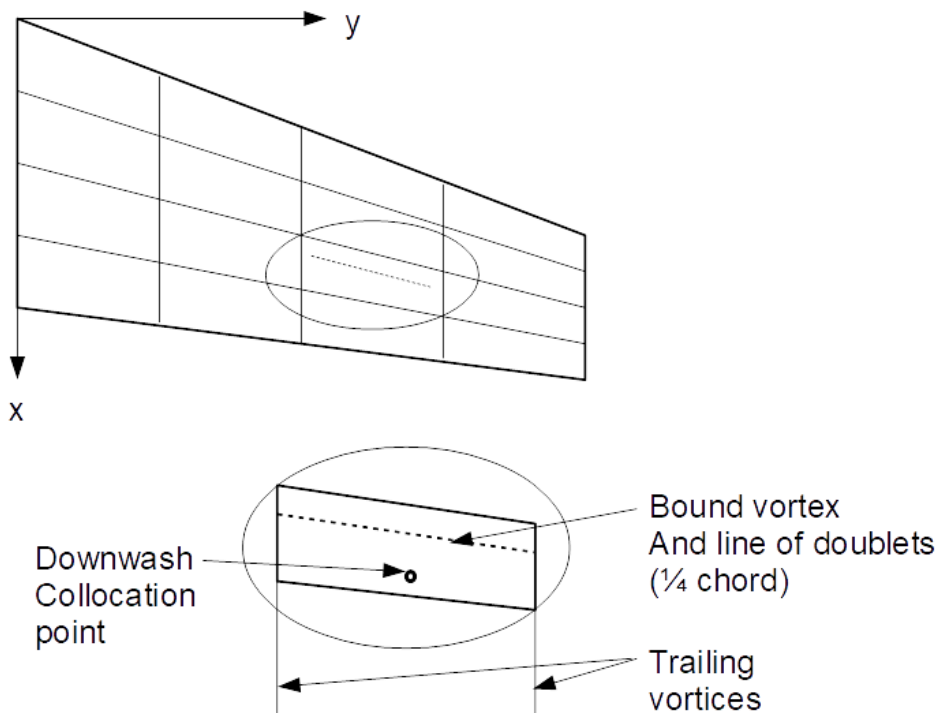


Figure 5-1: Discretization of the surface into doublet elements, with the positions of the collocation point and the bound vortex, adapted from [58]

The aerodynamic influence coefficient matrix is calculated by the following formulations:

$$[Q_{tt}] = [S_{tj}][A_{jj}]^{-1}[D_{jt}^1 + ikD_{jt}^2] \quad (5-14)$$

$$\{w_j\} = [A_{jj}]\{f_j/q\}, \quad (5-15)$$

$$\{w_j\} = [D_{jt}^1 + ikD_{jt}^2]\{u_t\} + \{w_j^g\}, \quad (5-16)$$

$$\{P_t\} = [S_{tj}]\{f_j\}, \quad (5-17)$$

where the components in turn are given by the three relations (5-15), (5-16) and (5-17)

containing:

- A_{jj} = aerodynamic influence coefficient matrix,
- S_{tj} = integration matrix,
- D_{jt}^1, D_{jt}^2 = Real and imaginary parts of substantial differentiation matrix,
- k = Reduced frequency,
- w_j = downwash,
- f_j = pressure on lifting element j ,
- q = flight dynamic pressure,
- w_j^g = static aerodynamic downwash,
- u_t = displacements at aerodynamic grid points,
- P_t = Forces at aerodynamic grid points.

Equation (5-15) represent the downwash, Equation (5-16) the differential matrix of deflection to obtain the downwash and Equation (5-17) the pressure integration to receive forces and moments, respectively. The Matrix Q_{tt} is then computed by decomposition as well as forward and backwards substitution.

The independence of the structural and aerodynamic grids allows each of them to be adapted optimal to the conditions and the chosen theory. However, as the two must exchange the acting forces on each, so called splines are used to fulfil this purpose. This connection is done by interpolation, where out of three methods can be selected:

- Linear splines;
- Surface splines;
- User defined interpolation.

For an aeroelastic model, all three methods can be picked in any combination. For long and slender bodies (as are high aspect ratio surfaces), the Nastran documentation recommends linear splines [42], which is why those were used. Later in the text, those will be explained in more detail.

In Nastran, the aerodynamic degrees of freedom are dependent, while the structural ones are independent. The coupling takes place through a derived matrix. In sum, two transformations are necessary, one that interpolates the structural to the aerodynamical deflections and another for the connection between the aerodynamic forces and the structurally equivalent forces occurring on the structural grid points. This leads to the interpolation matrix $[G_{tg}]$ relating the structural grid point deflections $\{u_g\}$ to the aerodynamic grid point deflections $\{u_t\}$:

$$\{u_t\} = [G_{tg}]\{u_g\}. \quad (5-18)$$

The structural and aerodynamic grids must interact and are connected by interpolation, which is done by so called splines. With this method, the deformation of the two models, structural and aerodynamical, is tried to match (“structurally equivalent”). This is more important rather than a statically equivalence, where the forces match but the deformations are not necessarily equal.

By applying this theory, the aerodynamic forces F_t and the structurally equivalent forces F_s acting on the structural grid points lead to the same virtual work:

$$\{\delta u_t\}^T \{F_t\} = \{\delta u_s\}^T \{F_s\}, \quad (5-19)$$

with the virtual deflections $\{\delta u_t\}$ and $\{\delta u_s\}$. By substituting (5-18) in (5-19) it can be obtained:

$$\{\delta u_s\}^T ([G_{ts}]^T \{F_t\} - \{F_s\}) = 0, \quad (5-20)$$

and because of the arbitrariness of the virtual deflections:

$$\{F_s\} = [G_{ts}]^T \{F_t\}. \quad (5-21)$$

Both Equations (5-18) and (5-21) are necessary to close the problem formulation for aeroelasticity, where the aerodynamic and structural grids do not match in first place. Further insight into the theory behind the surface and beam splines can be looked up in the Nastran documentation [42], here only a short overview will be given.

The linear spline is like a beam function $w(x)$, which goes with the twist $\phi_i = \phi(x_i)$ through the known deflections $w_i = w(x_i)$. In Figure 5-2 it is illustrated, how the aerodynamic grid points (t-set) and the structural grid points (s-set) are connected by the linear spline.

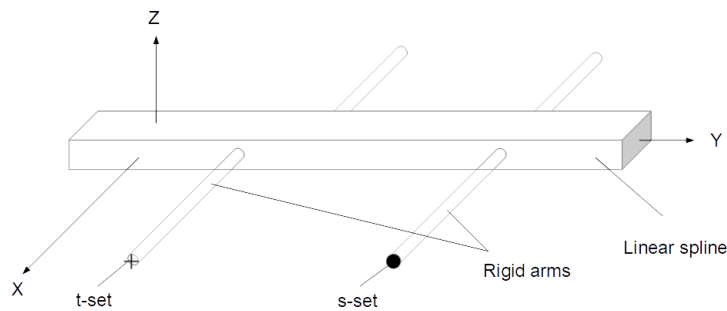


Figure 5-2: Beam spline for the structural and aerodynamic node connection

Flutter is a dynamic aeroelastic stability problem that occurs if the structural damping of a body is below zero. Which formulation is chosen to calculate flutter boundaries depends on how the aerodynamic loads are included in the aeroelastic equations and has to be compatible with the assumptions made. Several methods have been proposed to calculate the flutter speed, which are a transient method (named p-method by Hassig [44]), the k-method (also “American method”) by Theodorsen [26] and the p-k-method (“British Method”) developed by Hassig [44]. The k-method was developed to a more efficient method, the KE method, within MSC Nastran. Hodges and Pierce [45] compared the p, k and

p-k methods and as the p-k-method has proven itself adequate for flutter analysis, it was the chosen one for the calculations. Therefore, a short explanation of only this method is given next.

An aeroelastic dynamic problem can be formulated as:

$$[M]\{\ddot{x}\} + [C]\{\dot{x}\} + [K]\{x\} = \{F\}, \quad (5-22)$$

where $[M]$ is the mass matrix, $[C]$ the structure damping matrix, $[K]$ the structure stiffness matrix, $\{x\}$ the systems DOFs with its derivations and $\{F\}$ the load vector. The latter is the sum of the gravity force $[M]\{g\}$, the aerodynamic stiffness matrix $[A_K]$ and the aerodynamic damping matrix $[A_C]$:

$$\{F\} = [M]\{g\} + [A_K]\{x\} + [A_C]\{\dot{x}\}. \quad (5-23)$$

As MSC Nastran is used in this work and therefore a frequency approach for the flutter calculation is followed, their nomenclature will be used and explained following, according to [42].

The aerodynamic coefficient matrix $[Q_{kk}]$ from Equation (5-14) has to be altered to use in a flutter calculation. The necessary transformations are an appliance to the structural model by splines and a model reduction to reach the generalized form. This leads to the formulation:

$$[Q_{ii}] = [\Phi_{ai}]^T [G_{ta}]^T [WTFACT] [Q_{tt}] [G_{ta}] [\Phi_{ai}], \quad (5-24)$$

where

- Q_{ii} = Generalized aerodynamic matrix;
- Φ_{ai} = Matric of i-set normal mode vectors in the physical a-set;
- G_{ta} = Spline matrix reduced to a-set;
- $WTFACT$ = Matrix of empirical correction factors to adjust each theoretical aerodynamic box lift and moment to agree experimental data.

The solution can be obtained with the fundamental equation of the p-k method:

$$\left[M_{hh} p^2 + \left(B_{hh} - \frac{1}{4} \rho \bar{c} V Q_{hh}^I / k \right) p + \left(K_{hh} - \frac{1}{2} \rho V^2 Q_{hh}^R \right) \right] \{u_h\} = 0, \quad (5-25)$$

with following parts

- M_{hh} = Modal mass matrix;
- B_{hh} = Modal damping matrix;
- K_{hh} = Modal stiffness matrix;
- Q_{hh}^I = Modal aerodynamic damping matrix; imaginary part of $Q_{hh}(m; k)$;
- Q_{hh}^R = Modal aerodynamic stiffness matrix; real part of $Q_{hh}(m; k)$;
- p = Complex eigenvalue $\omega(\gamma \pm i)$;
- γ = Transient decay rate coefficient;
- \bar{c} = Reference length;
- ρ = Density;
- V = Velocity;
- k = Reduced frequency;
- $\{u_h\}$ = Modal amplitude vector.

Whereby the reduced frequency is dependent on the circular frequency by the relation:

$$k = \frac{\omega c}{2V}, \quad (5-26)$$

and furthermore:

$$k = (c/2V)Im(p). \quad (5-27)$$

By those expressions, Equation (5-25) can be rewritten for the p-k-method in state-space form with twice the order:

$$[A - pI]\{u_h\} = 0. \quad (5-28)$$

Now $\{u_h\}$ includes displacements as well as velocities. The eigenvalues of $[A]$ are either real or complex conjugate pairs. Real roots indicate a convergence or divergence as in the cases of the roll subsidence (rigid body) mode or a structural (torsional) [42]. For the real roots, the damping is expressed as the decay rate coefficient:

$$g = 2\gamma = \frac{2p\bar{c}}{(\ln 2)V}. \quad (5-29)$$

Yet most of the eigenvalues will be conjugate complex pairs and the oscillatory solutions of Equation (5-25) requires an iterative calculation in such a way that Equation (5-27) is satisfied together with Equation (5-25). The roll subsidence root or static structural divergence roots require no iteration and are found by setting $k = 0$. The oscillatory rigid body roots and oscillatory roots are found by an algorithm described in detail in [42]. However, the aim is to determine stability at a given speed independently of stability at lower or higher speeds. An advantage of using the p-k method is the production of results directly for a given set of velocities instead of necessary iterations to calculate the reduced frequency of flutter. Also, the estimated damping in the algorithm is more realistic than the pure mathematical expression of Equation (5-29).

5.3 MATLAB

For the generation of the input file (.bdf or .dat) for Nastran there are a variety of commercial programs (MSC Nastran, Siemens NX, FEMAP) on the market which include the creation, visualisation and postprocessing of a model besides the implemented Nastran solver. Because a MATLAB code already existed from a former thesis [46] and the program is a well-known tool it was adapted for the writing of the .bdf files for the Nastran solver. With the outputs from the MDO tool for the deflections and the beam properties all the required data can be written. For the evaluation of the results, MATLAB also was used to display results graphically.

5.4 SolidWorks

To use the generated data from the MDO tool for the CFD analysis, a CAD model was built with SolidWorks. As input served the aeroelastically deformed wing given by the position of the chord surface nodes discretized along the wingspan. The transition of the wing into the winglet was modelled by hand, curved to get a smooth transition. A fluid domain of one half of the wing and tail was built with the dimensions of 10x5x5 (length x width x height) times half wing span. Internally, a half-sphere was used for possible rotation with the centre at the centre of gravity of the whole aircraft. This was already done in regard of assumed upcoming dynamic simulations for rotation. As with this model only the longitudinal stability was investigated, a half model of the wing with the symmetry plane through the centre of gravity was taken to lower the computational cost.

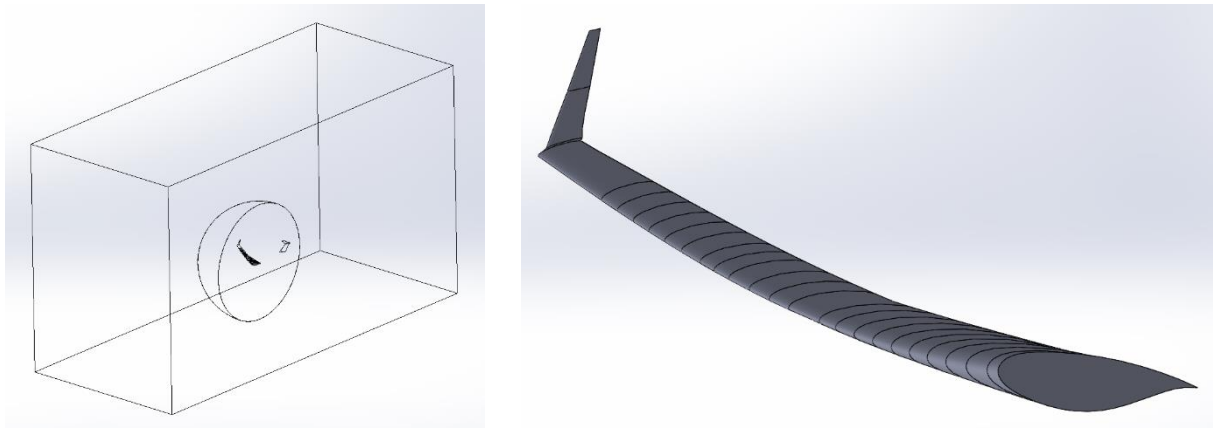


Figure 5-3: Wing and tail in the CFD environment and a sample of a deformed wing.

5.5 ANSYS

For the calculation of the stability derivatives the CFD tool ANSYS CFX was used. It is a well-known and commonly used program in the development process of aircrafts. The numerical method is based on the three-dimensional Navier-Stokes equation, which in the integral form can be written according to [47] as:

$$\frac{\partial}{\partial t} \iiint_V \vec{U} \cdot dV + \iint_S \vec{F} \cdot d\vec{S} = \vec{Q}, \quad (5-30)$$

where \vec{U} is the vector of conservation in the control volume V . The vector \vec{F} indicates the flux and \vec{Q} denotes the source term. The vector \vec{U} can be expressed as:

$$\vec{U} = \begin{bmatrix} \rho \\ \rho u \\ \rho v \\ \rho w \\ \rho \left[e + \frac{1}{2}(u^2 + v^2 + w^2) \right] \end{bmatrix}, \quad (5-31)$$

with the density ρ , the cartesian velocity components u, v, w and e is the specific energy. The source term is written as:

$$\vec{Q} = \begin{bmatrix} 0 \\ \rho g_x \\ \rho g_y \\ \rho g_z \\ \rho (u g_x + v g_y + w g_z) \end{bmatrix}. \quad (5-32)$$

Here, g_x, g_y and g_z is the gravity constant in the cartesian coordinate direction. In this work, Menter's Shear Stress Transport (SST) model [48] is used for modelling the turbulence. It combines the $k - \omega$ and the $k - \epsilon$ turbulence models and internally blends them with a factor, when the $k - \omega$ model is used in the near wall region and the $k - \epsilon$ in the far field region, respectively. For the meshing process, the Ansys workbench mesher was used, which generates an unstructured mesh. The setup of the mesh will be described in more detail in Chapter 9.1.

6 Model validation through Eigenvalues, Eigenvectors and single load displacements

The original model was provided as a Nastran stick model. For all the calculations, the properties of this model were extracted and taken as input into the MDOGUI. The output data of the MDOGUI was then reinstated into Nastran, with the help of a MATLAB script, to calculate the flutter speeds. To verify the accuracy of the newly created model, a comparison with the original model of Bombardier regarding eigenfrequencies and deformation took place. In Table 6-1 one can see that the eigenfrequencies of the two models are close together, the minor differences could be explained by small position inaccuracies due to rounding errors of the digits. Therefore, the implementation of dimensions, masses and inertias can be assumed as valid.

| Nr. | Mode shape | Eigenfrequencies [Hz] | | Error [%] |
|-----|----------------|-----------------------|--------------|-----------|
| | | Bombardier model | Matlab model | |
| 1 | First Bending | 2.7731 | 2.7741 | 0.03 |
| 2 | First Chord | 8.8975 | 8.9004 | 0.03 |
| 3 | Second Bending | 9.2646 | 9.2662 | 0.02 |
| 4 | First Torsion | 19.5355 | 19.5424 | 0.03 |
| 5 | Third Bending | 20.3099 | 20.2921 | 0.09 |
| 6 | Second Chord | 27.5683 | 27.5618 | 0.02 |
| 7 | Second Torsion | 32.2450 | 32.2349 | 0.03 |
| 8 | Fourth Bending | 36.8855 | 36.8206 | 0.18 |
| 9 | Third Torsion | 44.6031 | 44.4392 | 0.37 |
| 10 | Fifth Bending | 55.8265 | 55.6963 | 0.23 |

Table 6-1: Comparison of the Eigenfrequencies

For validating the displacement accuracy, two single point loads were chosen, one in z-axis direction, the other in x-axis direction. Those were selected as they are the lift and the drag directions, respectively. The load was applied at the node where the second part of the wing starts, and the displacement was then taken at the wingtip. They were performed as static loads without any influence of the aerodynamic model, since only the structural model was used. The load value was chosen in such a way that it deforms the wing high enough to have a reasonable and comparable displacement. Hence, the load in the in-plane direction is a factor 100 higher than in the z-direction. The load applied was $1 \times 10^6 N$ for the in-plane bending and $1 \times 10^4 N$ for the out-of-plane bending, respectively. Furthermore, the displacement due to gravity as a constant load over the wingspan was checked up as displacement at the wingtip. Also, a moment around the y-axis was applied to see if pitching moments will give the same results. The value of the moment was $1 \times 10^6 Nm$ to get a well comparable displacement as well as for the single point loads. This was done at the same point as for the loads and the results were taken from the wingtip. All those can be seen in Table 6-2.

In sum, the eigenfrequencies do match well with a maximum difference under 0.4%. For the applied loads, one can recognize the good accordance for the deflections in the z-direction, which will be of the

most importance. For the moment around the y-axis (pitch) and the displacement in the x-direction (in wing plane), the errors are higher, around 5 and 7 percent, respectively. This could be caused by different reasons. One can be inaccuracies in the model due to rounding errors in the digits, another can be a slightly different approach for the beam elements of Nastran and the MDO tool. The original Nastran model is based on BAR elements, while the MDO structural model is based on BEAM elements. For the current work, the difference of under ten percent is seen as reasonable, especially as comparisons of results will only be made with the output models of the MDO tool.

| Displacements | | | |
|---|------------------|--------------|-----------|
| | Bombardier model | Matlab model | Error [%] |
| Displacement x-direction [m] due to force in x-direction | 0.1911 | 0.1772 | 7.27 |
| Displacement z-direction [m] due to force in z-direction | 0.2372 | 0.2368 | 0.15 |
| Displacement z-direction [m] due to gravity force | 0.0632 | 0.0631 | 0.11 |
| Rotation angle around y-axis [°] due to moment around y axis | 0.1416 | 0.1486 | 4.91 |

Table 6-2: Comparison for validation of the Bombardier and the MATLAB model

7 Linear and nonlinear structural deflections and its effect on flutter speed

To see the influence of nonlinear calculations on deflections, a comparison between the displacements of the wingtip with linear and nonlinear calculation will be presented next. All those simulations were carried out as steady state simulations without accounting for dynamic load changes, i.e. like gust or high g manoeuvres. In Figure 7-1, an overview of the process is given.

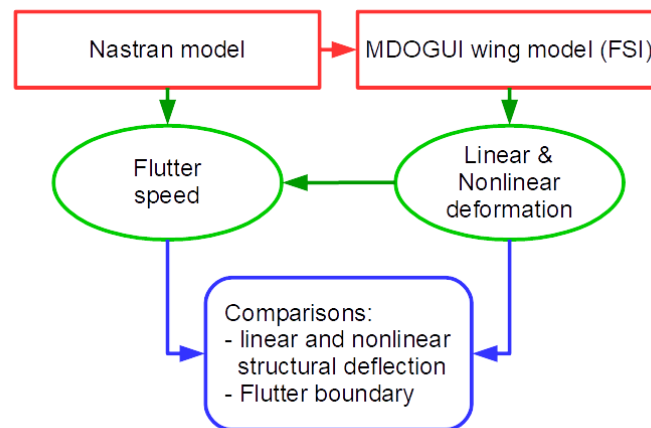


Figure 7-1: Process of calculations for the displacements and the flutter speed

For a first approach, different flight conditions were chosen to calculate the deformation within the MDOGUI. This was done to examine the calculation time for the different angles of attack, velocities and altitudes as well as the deformations. During those calculations, it could already be seen that higher deformations occur for higher angles of attack, higher velocity and lower altitudes. However, the calculation time also increased with those factors and a balance had to be found between computational cost and flight conditions. In that context, the airspeed was taken constant during the following simulations at a value of 200 m/s, as the speed was closer to the operating conditions and the calculation time was still low enough.

As listed in Table 7-1, with a higher deflection the difference between a linear and a nonlinear calculation increases. However, the difference is small, as is the displacement for both cases (under 10 % of semi wing span).

The calculations were done with an angle of attack of 5° and at altitudes ranging from 12497m, which corresponds to 41000 ft, down to an imaginary altitude of -1000 m, where due to the higher density larger displacements could be achieved. As one can see, the deformation itself is not extraordinary high. The wing of interest is classified in the beginning as high aspect ratio wing, but compared with other research objects, for example HALE aircraft [49, 50], can be seen on the lower border of that classification. Therefore, very high displacements were not expected to be observed.

| Altitude | Linear displacement [m] | | Nonlinear displacement [m] | | relative Difference between linear and nonlinear displacements |
|----------|-------------------------|----------------------|----------------------------|----------------------|--|
| | absolute | rel. to half span | absolute | rel. to half span | Δ |
| 12497 m | 0.3895 m | 3.10 % | 0.3876 m | 3.08 % | 0.49 % |
| 6000 m | 0.6716 m | 5.33 % | 0.6629 m | 5.26 % | 1.31 % |
| 5000 m | 0.7117 m | 5.65 % | 0.7014 m | 5.57 % | 1.44 % |
| 4000 m | 0.7485 m | 5.94 % | 0.7365 m | 5.85 % | 1.52 % |
| 3000 m | 0.7843 m | 6.22 % | 0.7700 m | 6.11 % | 1.77 % |
| 2000 m | 0.8185 m | 6.50 % | 0.8022 m | 6.37 % | 2.00 % |
| 1000 m | 0.8491 m | 6.74 % | 0.8292 | 6.58 % | 2.37 % |
| 0 m | 0.8753 m | 6.95 % | 0.8521 m | 6.76 % | 2.73 % |
| -1000 m | 0.8956 m | 7.11 % | 0.8711 m | 6.91 % | 2.81 % |

Table 7-1: Deformation comparison at different altitudes for constant angle of attack and velocity; deformation data for an angle of attack of 5° and 200 m/s

In Figure 7-2, the dimensionless vertical displacement can be seen as a function of the dynamic pressure. The velocity was set constant and the dynamic pressure is decreasing with increasing altitude.

A trend is recognizable for an increasing difference between the linear and nonlinear calculations of the displacements as higher they get. In sum, the displacements in a steady flight condition are not extraordinary high. However, for dynamic conditions, e.g. gust response, the displacements could be higher and the influence of nonlinear geometric behaviour could be more severe. The influence in the calculated flutter speed will be discussed later.

Dimensionless displacement over dynamic pressure (200 m/s deformation data, 5°AoA)

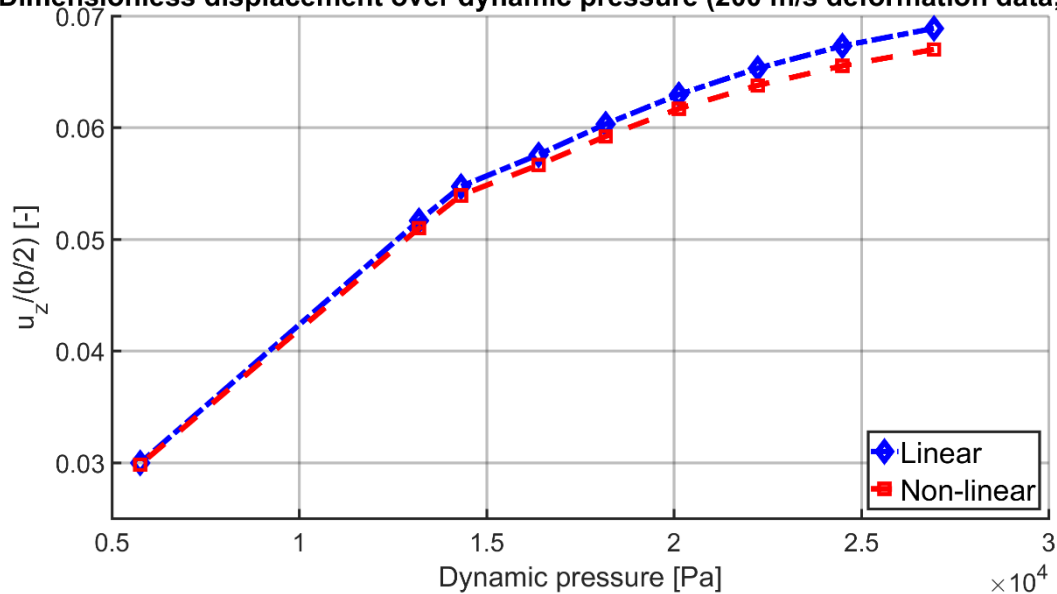


Figure 7-2: Comparison of linear and nonlinear displacement in dependency of the dynamic pressure

A second comparison was made for the displacement in dependency, where the angle of attack was varied. Here, it also can be noticed that with an increasing angle the deflection increases (see Table 7-2 and Figure 7-3). The same as in the case before, the difference between the linear and the nonlinear displacement increased with higher deflections, although it is not very high.

| Angle of attack | Linear displacement | | Nonlinear displacement | | relative Difference between linear and nonlinear displacements |
|-----------------|---------------------|----------------------|------------------------|----------------------|--|
| | absolute | rel. to half span | absolute | rel. to half span | Δ |
| -2° | -0.7800 m | 6.19 % | -0.7539 | 5.98 % | 3.39 % |
| 0° | -0.3158 m | 2.51 % | -0.3044 | 2.42 % | 3.60 % |
| 2° | 0.1594 m | 1.26 % | 0.1591 | 1.26 % | 0 % |
| 4° | 0.6361 m | 5.05 % | 0.6229 | 4.94 % | 2.18 % |
| 5° | 0.8753 m | 6.95 % | 0.8521 | 6.76 % | 2.73 % |
| 6° | 1.1081 m | 8.79% | 1.0746 | 8.53 % | 2.96 % |
| 8° | 1.5636 m | 12.41 % | 1.4939 | 11.86 % | 4.43 % |
| 10° | 1.9841 m | 15.75 % | 1.8728 | 14.86 % | 5.65 % |

Table 7-2: Deformation comparison of different angles of attack at constant altitude and velocity; deformation data for sea level at 200 m/s

Up to a displacement of 10% of the halfspan, the difference is relatively small, then, the influence of nonlinear effects increase. Here, nonlinear strain-displacement kinematics and follower forces play a role in the restoring forces in a wing and leads to lower deflections. Even higher dissimilarities could be expected with higher displacement. As stated in [38], the tip displacement has an influence on the flutter speed, and therefore the deformation will change the speed for which flutter begins.

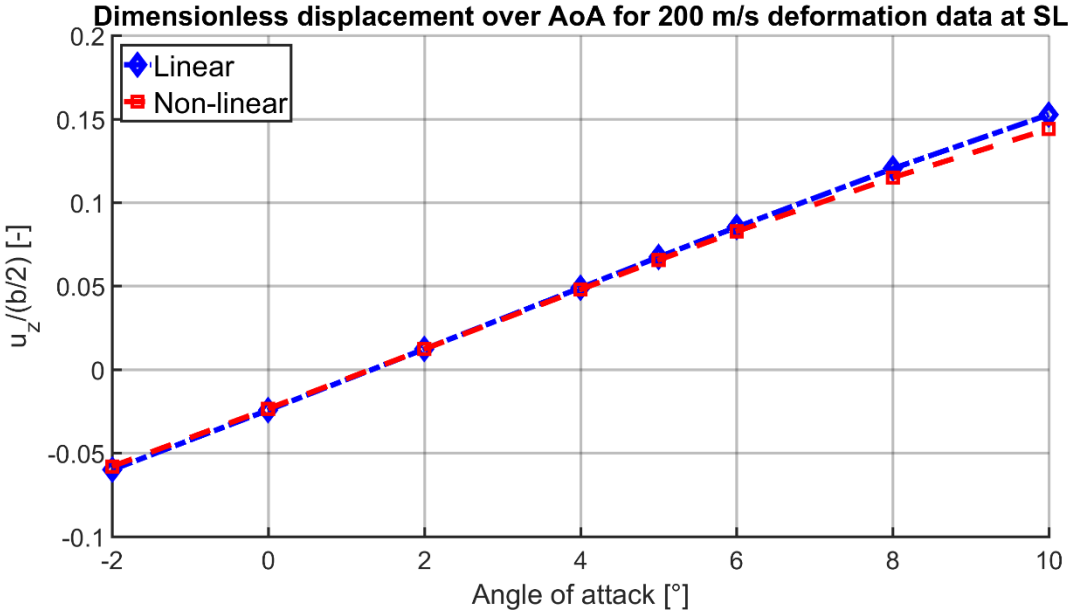


Figure 7-3: Comparison of linear and nonlinear displacement for increasing angle of attack

In sum it can be recognized that the influence of nonlinear structural behaviour is not excessive for the flight conditions the aircraft is supposed to operate in steady state flight. For the dynamic behaviour, at

this point it cannot be predicted, if the influence of nonlinearities is much higher (for example due to gusts).

Eigenfrequencies

To see the influence of deformation in general and the comparison between linear and nonlinear structural displacements, an analysis of the eigenfrequencies will be shown here. Due to the different flight conditions, in terms of angle of attack, airspeed and altitude, different deformations for the non-rigid wing are obtained. As a criterium for that, the wing tip displacement (before the winglet begins) can be taken. In Figure 7-4 the trend for the eigenfrequencies over the tip displacement can be seen for the linear and the nonlinear wings. In Figure 7-5 a) -j), a finer contemplation was done to show the proportional change of the linear and the nonlinear deformations.

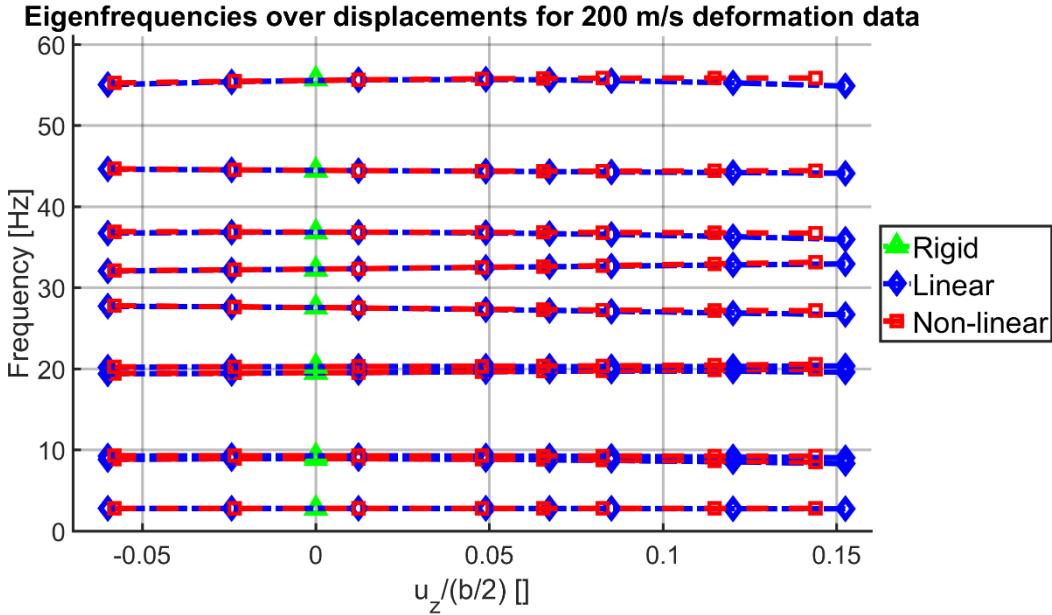
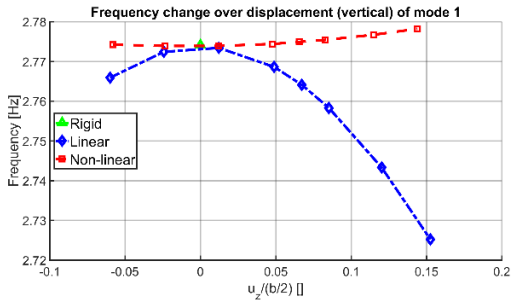
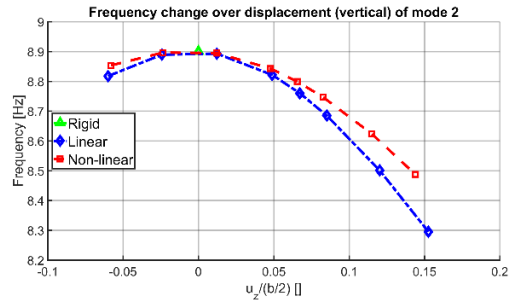


Figure 7-4: Eigenfrequencies of the first 10 modes for the rigid, linear and nonlinear wing

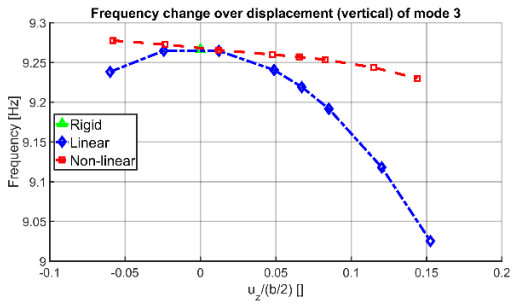
One can recognize, that the change neither for the linear nor for the nonlinear deformed wing is extraordinary high. In the detailed views, some differences and trends can be noticed between the two deformed wings. The modes 1, 3 and 8 have a relatively low slope for the nonlinear deformed wing, while the linear deformed one changes more recognizable. Modes 2, 5 and 7 have a trend alike each other, while the modes 4, 6, 9 and 10 have an opposite trend regarding linear and nonlinear displacement, with diverging eigenfrequencies. However, the change in the eigenfrequencies is not very high, being under 2% for bending and torsion modes and 4% and 7% for the in-plane modes, respectively.



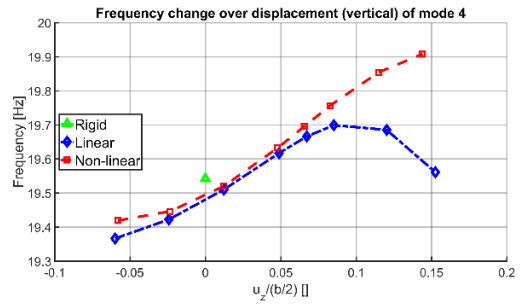
(a) First Bending



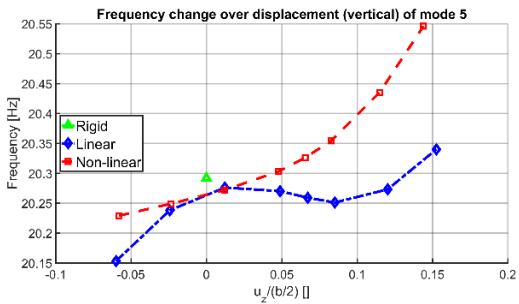
(b) First Chord



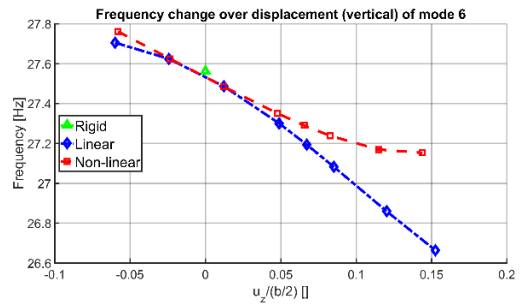
(c) Second Bending



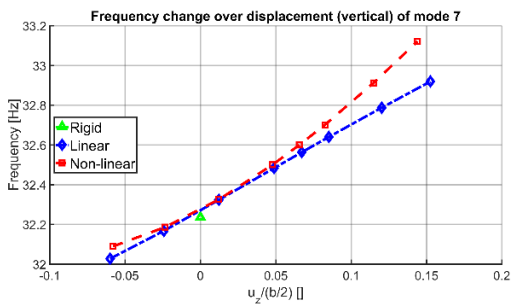
(d) First Torsion



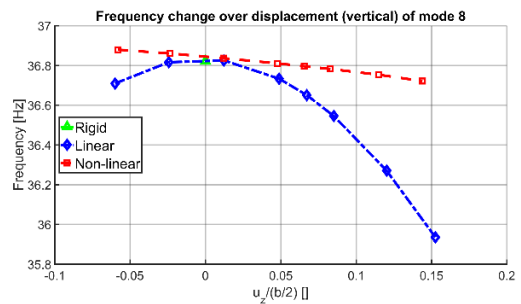
(e) Third Bending



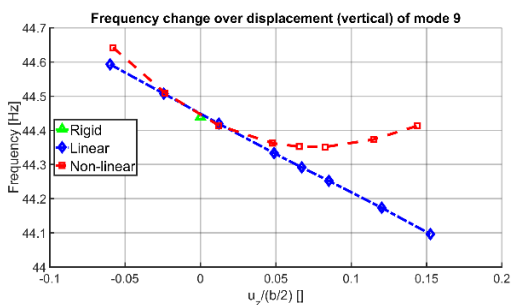
(f) Second Chord



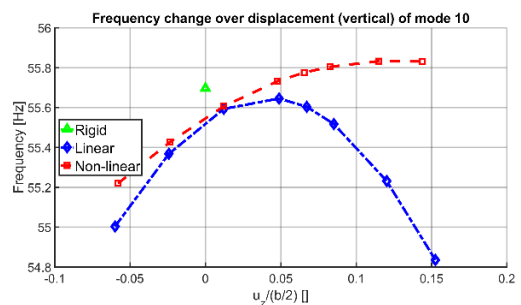
(g) Second Torsion



(h) Fourth Bending



(i) Third Torsion



(j) Fifth Bending

Figure 7-5: First 10 modes with corresponding frequency changes

Flutter

Next, the calculation of the flutter speed for the wing will be described and the achieved results will be discussed.

For the flutter speed calculation setup, the range of interest was set between 0 m/s and 350 m/s. The reason for this choice is the existence of the sound barrier, as the chosen aerodynamic theory for the flutter calculation is the Doublet Lattice Method (DLM), which is only valid for subsonic cases. Hence, every result above the speed of sound as flutter solution should be taken with caution. The reduced frequency was set between 0.01 and 7 to cover the steady state range as well as the highly unsteady range.

As it was not sure in the beginning, where the flutter boundary will be and how it behaves, a test matrix was worked out for a variation of angle of attack (2° , 5° and 10°), airspeeds (100 m/s, 150 m/s and 200 m/s) and altitudes (0m and 12497m). Especially for 5° angle of attack, several additional altitudes were added (from -1000m to 6000m) to examine the appearing of the flutter boundary regarding altitude. Throughout the initial calculations, it was noticeable that an air speed around 200 m/s is a good compromise for a speed as high as possible, while the calculation is done in a reasonable amount of time.

An exemplary result for 10° angle of attack for the linear deformed wing is presented in Figure 7-6 and Figure 7-7. The damping for the first bending mode (mode 1) and the second bending mode (mode 3) increase with velocity. At around 250 m/s the gradient of the damping of both modes increases. After a short drop, the damping of mode 3 tends to converge. With increasing velocity, the frequency of mode 1 becomes zero at around 325 m/s, indicating the appearance of divergence. Until this speed, the damping of mode 1 diverges. When its frequency drops to zero, its damping also jumps and, despite still being negative, has a positive gradient. While the damping for the modes 1 and 2 increase, the first in-plane mode (mode 2) and the first torsion mode (mode 4) change from a negative damping gradient to a positive one, until they become undamped at some point. Mode 4 diverges after getting a positive damping while mode 2 only achieves a low positive damping and its gradient even becomes slightly

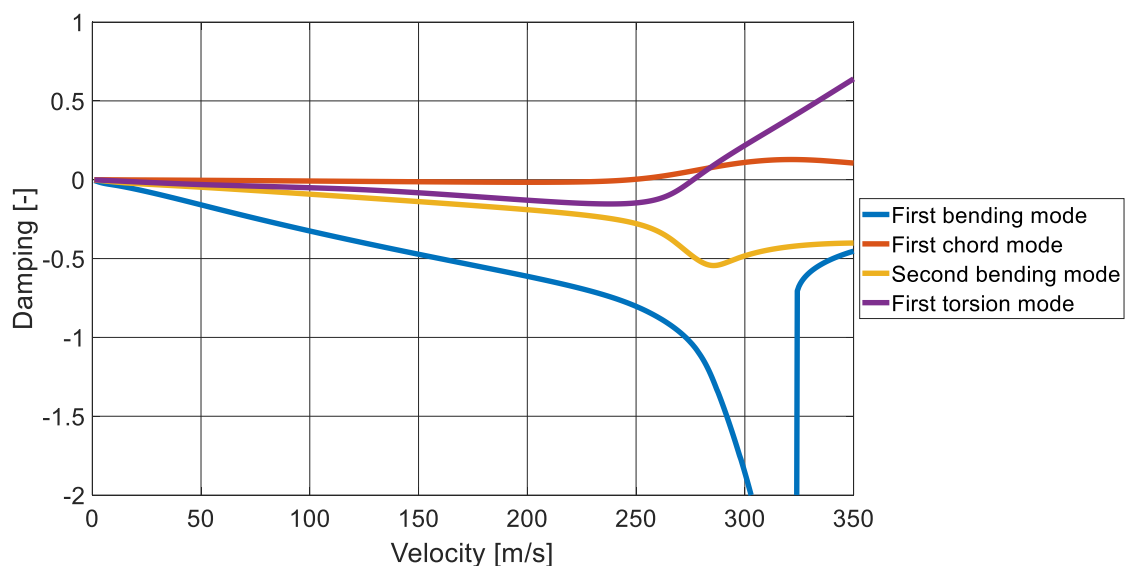


Figure 7-6: Damping graph for one of the flutter analysis

negative again with increasing velocity. In this exemplary case, mode 2 is the first flutter mode, appearing at 247.19 m/s and mode 4 becomes unstable at 275.86 m/s. While it is not ascertainable which modes exactly couple, it could be assumed that the first bending mode and the first torsion mode couple due to the distinct frequency change (what would imply the more common bending-torsion-flutter). To determine if the chord flutter actually occurs earlier, experiments should be considered.

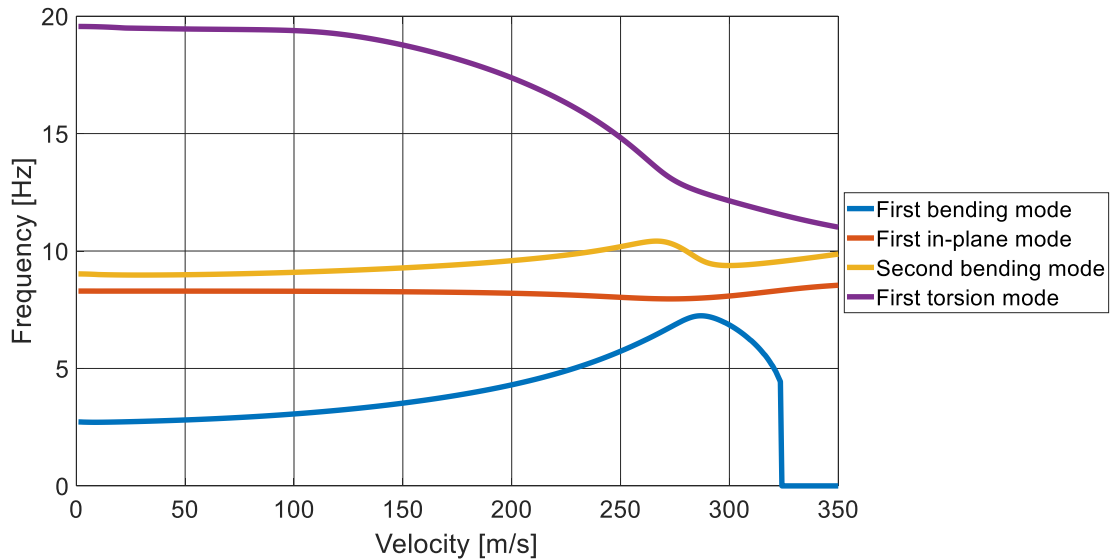


Figure 7-7: Frequency graph for one of the flutter analysis

The flutter speeds from the single calculation results are given in Figure 7-8.

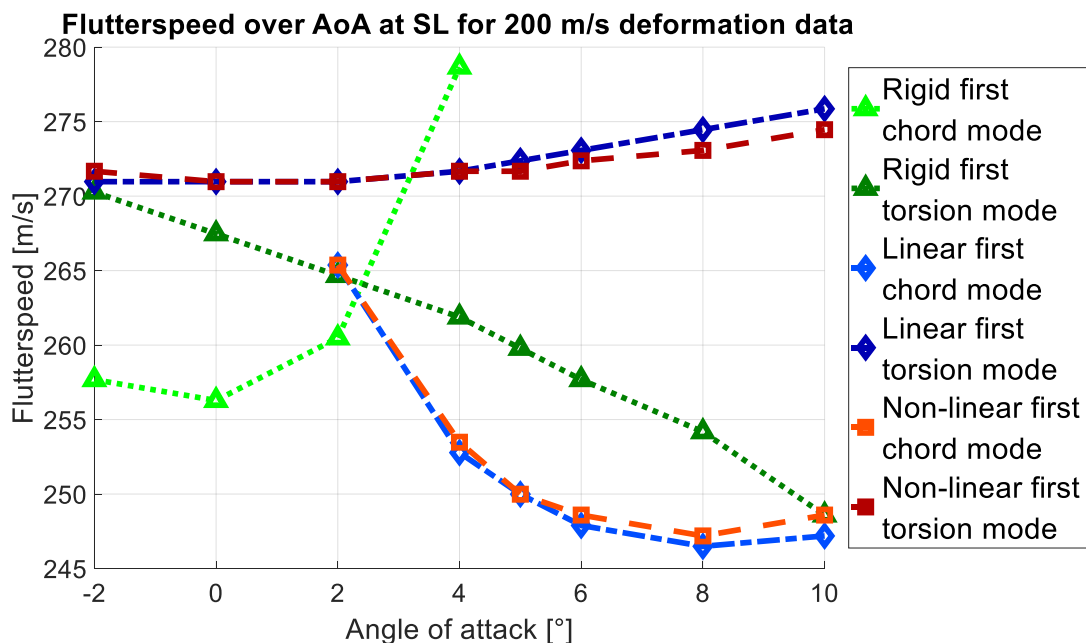


Figure 7-8: Flutter speed depending on angle of attack for the rigid, linear deformed and nonlinear deformed wing at an altitude of 0m (sea level)

Here, different conclusions could be drawn:

- (1) The flutter boundary does not appear in the examination range above an altitude of 6000m (see **Fehler! Verweisquelle konnte nicht gefunden werden.**). It should be mentioned, that flutter

speed results above the speed of sound should be taken with care, as the theory of DLM, as stated before, is supposed to model the aerodynamics within the sub- and transonic regimes.

- (2) The flutter speed for the same angle of attack, altitude and speed is slightly higher for the nonlinear deformed wing than for the linear deformed one for the in-plane mode (see Figure 7-8). An explanation for that is the lower structural vertical displacement of the former one for these flight conditions due to the geometrical shortage of the effective wing span and the resulting lower lift. Also, horizontal displacement seems to have an influence. The nonlinear wing deforms more in the in-plane direction, which could lead to a lower flutter speed. which displacement the stronger influence has, might be a topic of further investigations.
- (3) The flutter speed decreases with higher structural displacements for the in-plane mode. For increasing angles of attack as well as lower altitudes, the deformation of the wing increases and therefore the flutter speed decreases. For the torsion mode, the wing twist increases with increasing angle of attack, which seem to have an opposing influence on the flutter speed. This could be an explanation of the increasing flutter speed for this mode. Further examination has to be done here for more detail.
- (4) The flutter mode for the rigid wing is the first chord mode for small angles of attack and changes to the first torsion mode for higher angles of attack. Opposing to that behaviour is the flutter boundary of the flexible wings, where the flutter mode changes from the first torsion mode to the first chord mode for increasing angles of attack.
- (5) Even though the flexible wing starts fluttering earlier for high angles of attack within the chord mode, a remarkable behaviour is noticeable for the torsional mode of the wing. While the slope of the flutter speed for the rigid wing is negative, the flexible wings have a behaviour in the complete opposite direction. This indicates a high correlation between even small torsional deformations and the flutter behaviour.

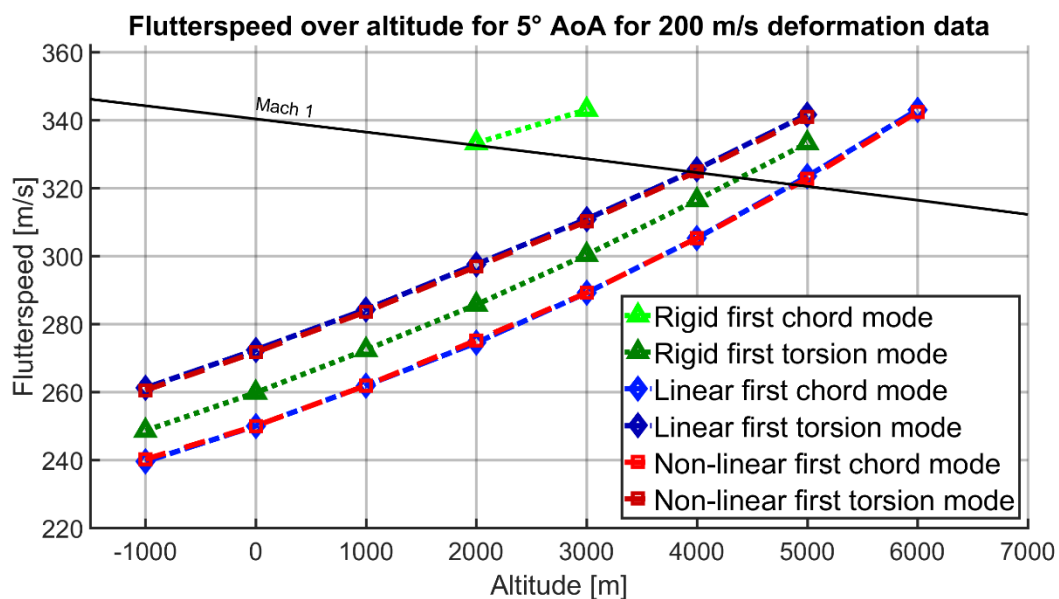


Figure 7-9: Flutter speed for increasing altitude at an angle of attack of 5°

8 Parametric study

An examination regarding a structural parameter took place. Usually, the structure of the wing is executed as a wing box, as it has the advantage of structural stiffness, low weight and enough space for necessary non-bearing structure. For instance, this can include tanks, electronics or shafts. With that in mind, it was in the scope of interest, how and with what magnitude the performance of the wing would change, if a geometrical change in the wing box structure will take place. The background for those calculations was to archive higher displacements of the wing, not taking into account the stress in the wing (meaning the wing could fail even before reaching a specific deformation). For that, first some assumptions were made to simplify the calculations:

- The wing box consists of a rectangular box with a width B , a height H and a thickness t ; the box is not shaped like the airfoil, as it would be without the simplification. In Figure 8-1 the box is shown and the airfoil shape is indicated as the dashed line.
- The dimensions of the wing box are the full height of the section and half of the section's chord as width;
- t is around two orders of magnitude smaller than B and H , meaning $t \ll B, H$; this assumption can be validated by a rough estimation with the given data. For an arbitrary cross-section of the wing, about 50% of the chord length can be assumed for the wing box width and the whole height of the section for the box height. With those dimensions and the given area of the cross-section, the estimated thickness is for all wing sections around 5mm. Thus, compared with the height and width, the thickness is around two magnitudes smaller than the other dimensions¹. In Figure 8-1 the simplified wing box can be seen with the airfoil shape as the dashed line around the box.
- As mentioned already, the stress was not monitored for the study. Therefore, even if the resulting stress exceeds the material capability, the wing is assumed not to fail.

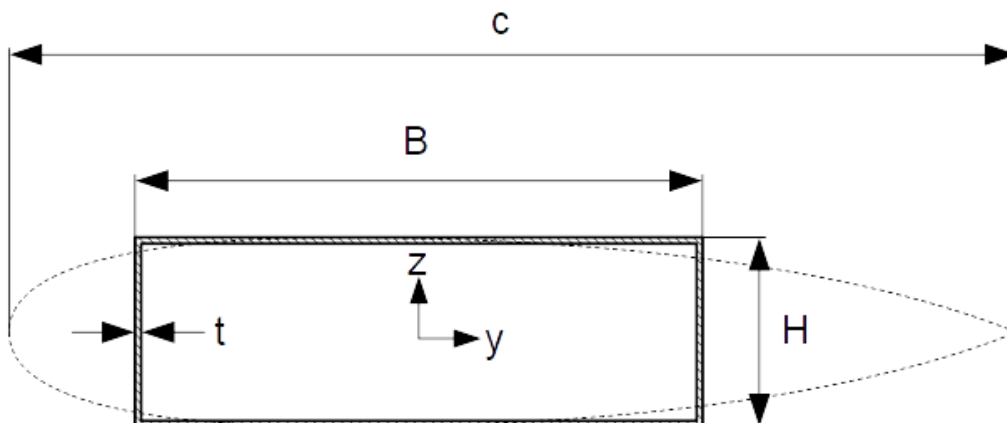


Figure 8-1: Idealized wing box with the dashed shape of the airfoil around, simplified for a rectangular wing box; with the chord c , the wing box height H , wing box width B and thickness t

¹ For instance, for the wing root: Chord length of 4.5m leads to a wing box width of 2.25m and the height is around 17% of the chord length (0.75m). With an area of 0.03m² this leads to a thickness of 0.005m.

The objective of the parametric study would be to reduce the mass (structural mass) of the wing. As the mass is dependent on the volume and the density of the structure, and the span as well as the material will stay the same, the area of a cross-section would be reduced. With the restrictions of the airfoil shape, the values of B and H will stay the same, so only the thickness will be reduced. This will happen by a factor of increase or decrease, where the new thickness $t^* = k \cdot t = t + \Delta t$. With this, there also follow some changes for the other geometrical characteristics, such as the area moment of inertia (I_{yy}, I_{zz}), torsional stiffness constant (J), mass moment of inertia ($I_{xx}, I_{yy}, I_{zz}, I_{xy}, I_{xz}, I_{yz}$).

The area of the wing box' cross-section A can be correlated with its thickness by:

$$A = 2(Bt + Ht - 4t^2) \approx 2(B + H)t. \quad (8-1)$$

With the simplification of the small ratio of t to B and H the last term can be neglected and therefore a linear dependency of the area to the thickness can be assumed:

$$A \sim t. \quad (8-2)$$

Therefore, the changed area A^* can be expressed by:

$$A^* = k \cdot A. \quad (8-3)$$

For the area moment of inertia, it applies:

$$I_{yy} \approx 2 * \left(\frac{1}{12} tH^3 + \frac{1}{12} t^3 B + \left(\frac{H-t}{2} \right)^2 * tB \right), \quad (8-4)$$

and with the assumption of $t \ll B, H$:

$$I_{yy} \approx \frac{1}{6} tH^3 + \left(\frac{H}{2} \right)^2 * tB = \left(\frac{1}{6} H^3 + \frac{1}{4} H^2 B \right) t, \quad (8-5)$$

from which follows:

$$I_{yy} \sim t, \quad (8-6)$$

$$I_{yy}^* = k \cdot I_{yy}. \quad (8-7)$$

It is the same for I_{zz}^* , which is also proportionally dependent. For the torsional constant, the formula for torsional stiffness is taken [51]:

$$J = \frac{4A_E^2}{\oint \frac{ds'}{t}} \quad (8-8)$$

where A_E is the area surrounded by the closed box profile regarding its centre line. This area is approximately:

$$A_E = (B - t)(H - t) \approx BH, \quad (8-9)$$

when taking into account that $t \ll B, H$. As we also assume a constant t around the box, J is directly proportional to t , as the integral $\oint ds$ is the perimeter of the box:

$$J \approx \frac{4A_E^2}{2(B+H)}t. \quad (8-10)$$

The mass of the wing consists of two parts: the structural mass, responsible for stability, and the mass of the already assumed additional applications (e.g. shafts, skin). As the mass of the wing is given by mass points only, the structural mass was calculated by the density of the material, the cross-section areas and the length of the single sections by:

$$m_{str} = \sum A_i * l_i * \rho. \quad (8-11)$$

The whole mass is the sum of the mass points:

$$m_{tot} = \sum m_{points} = m_{str} + m_{add} = \frac{m_{str}}{m_{tot}}m_{tot} + \left(1 - \frac{m_{str}}{m_{tot}}\right)m_{tot}. \quad (8-12)$$

The fraction of the structural mass can then be expressed following:

$$f = \frac{m_{str}}{m_{tot}}. \quad (8-13)$$

With this fraction factor, the wing mass can be estimated as:

$$m_{tot} = fm_{tot} + (1-f)m_{tot}. \quad (8-14)$$

The new mass is dependent on the new structural mass and the same additional mass:

$$m_{tot}^* = m_{str}^* + m_{add} = k m_{str} + (m_{tot} - m_{str}) = (k-1)m_{str} + m_{tot} \quad (8-15)$$

Therefore, the mass fraction between the two different structures is:

$$\frac{m_{tot}^*}{m_{tot}} = \frac{(k-1)m_{str} + m_{tot}}{fm_{tot} + (1-f)m_{tot}} = \frac{f(k-1) + 1}{f + (1-f)} = 1 - (1-k)f. \quad (8-16)$$

Hence, the changed total mass is dependent on the initial fraction of the structure and the additional mass, as well as on the thickness. In this specific case, the mass ratio is 0.73, which means, for a thickness decrease of 10%, the total mass would only decrease for 7.3%.

In sum, all the changing geometric parameters are estimated by a direct linear proportionality of the thickness t and the structural mass. Taking into account the additional mass, a lower change factor for the mass will result:

$$A, J, I_{yy}, I_{zz} \sim t, \text{ with } k = 1, \quad (8-17)$$

and:

$$m_{ges}, I_{xx}, I_{yy}, I_{zz}, I_{xy}, I_{xz}, I_{yz} \sim t \text{ with } k^* = [1 - (1-k)f]. \quad (8-18)$$

Those changed values were put into the MDOGUI, several calculations were made to get the new displacements, and the flutter speeds were calculated with Nastran.

In Figure 8-2 the flutter speeds of the wings with the lower thicknesses are shown together with the flutter boundary of the wing with the original values. The Flutter boundaries for the in-plane mode and the torsion mode are drawn separately for a better overview. A noticeable difference can be seen, where the difference is around 5% for the flutter speed for the 10% thickness reduction and 10% for the 20% reduction. The trend of the flutter boundary is the same for the reduced thickness, as expected. For the deformations, the vertical displacements are around 3% for higher angles of attack and up to 10% for low angles of attack (and therefore low displacements) for the 90% thickness box. That means that the influence of a reduction of the wing box thickness by a tenth, results in a decrease of flutter speed by approximately 5%. For the decrease in thickness of 20% ($t'=0.8t$), the behaviour is likewise, but with a displacement difference of 25% for low angles of attack and 6% for the higher. Same as for originally geometric values, the deformation of the nonlinear deformed wing is less than the linear deformed one, as well as the flutter is speed is higher. An overview about the values obtained is given in Table 8-1 and Table 8-2 for the displacement, and in Table 8-4 to Table 8-6 for the flutter speeds, respectively.

| Angle of attack [°] | u_{z_t} [m] | $u_{z_{0.9t}}$ [m] | $ \Delta $ [%] | $u_{z_{0.8t}}$ [m] | $ \Delta $ [%] |
|---------------------|---------------|--------------------|----------------|--------------------|----------------|
| -2 | -0.780 | -0.853 | 9.36 | - | - |
| 2 | 0.159 | 0.143 | 10.06 | 0.117 | 26.42 |
| 6 | 1.108 | 1.149 | 3.70 | 1.187 | 7.13 |
| 10 | 1.984 | 2.071 | 4.39 | 2.164 | 9.07 |

Table 8-1: Differences in vertical displacement for the reduced box thickness for the linear deformations

| Angle of attack [°] | u_{z_t} [m] | $u_{z_{0.9t}}$ [m] | $ \Delta $ [%] | $u_{z_{0.8t}}$ [m] | $ \Delta $ [%] |
|---------------------|---------------|--------------------|----------------|--------------------|----------------|
| -2 | -0.754 | -0.819 | 8.62 | - | - |
| 2 | 0.159 | 0.143 | 10.06 | 0.119 | 25.16 |
| 6 | 1.075 | 1.108 | 3.07 | 1.141 | 6.14 |
| 10 | 1.872 | 1.944 | 3.85 | 2.017 | 7.75 |

Table 8-2: Differences in vertical displacement for the reduced box thickness for the nonlinear deformations

It comes to attention, that for higher angles of attack the tip displacement increases with a reduction of the thickness, while for lower angles, the tip displacement decreases. This can be explained by the following two factors: with the reduction of the thickness the torsional stiffness as well as the mass is reduced; however, the mass reduction is smaller, as the additional masses stay the same and only the structural mass is reduced; as the airfoil has a downwash and the torsional stiffness decreases, the torsion is increased. This leads to a reduction of the effective angle of attack, especially for low angles. Hence, the lift is reduced at the wing tip, leading to a lower displacement. Opposing to the wing tip trend, in the mid wing section, a displacement rise can be seen throughout the thickness reduction. In simplified terms, the wing shapes more like a gull wing with the thickness decrease of the wing box.

The same as for the linear deformations applies for the nonlinear deformations. The mid wing section has an increasing vertical displacement, while the wing tip has a lower one for small angles of attack.

| Angle of attack [°] | $v_{Fl,t}$ [m] | $v_{Fl,0.9t}$ [m] | $ \Delta $ [%] | $v_{Fl,0.8t}$ [m] | $ \Delta $ [%] |
|---------------------|----------------|-------------------|----------------|-------------------|----------------|
| 2 | 265.37 | 256.28 | 3.43 | 248.59 | 6.32 |
| 6 | 247.89 | 233.20 | 5.93 | 223.41 | 9.88 |
| 10 | 247.19 | 235.30 | 4.81 | 219.21 | 11.32 |

Table 8-3: Flutter speeds for the reduced box thickness for the linear deformed wing for the first in-plane rigid body mode

| Angle of attack [°] | $v_{Fl,t}$ [m] | $v_{Fl,0.9t}$ [m] | $ \Delta $ [%] | $v_{Fl,0.8t}$ [m] | $ \Delta $ [%] |
|---------------------|----------------|-------------------|----------------|-------------------|----------------|
| 2 | 265.37 | 256.28 | 3.43 | 248.59 | 6.32 |
| 6 | 248.59 | 236.70 | 4.78 | 224.81 | 9.57 |
| 10 | 248.59 | 236.70 | 4.78 | 224.11 | 9.85 |

Table 8-4: Flutter speeds for the reduced box thickness for the nonlinear deformed wing for the first in-plane rigid body mode

| Angle of attack [°] | $v_{Fl,t}$ [m] | $v_{Fl,0.9t}$ [m] | $ \Delta $ [%] | $v_{Fl,0.8t}$ [m] | $ \Delta $ [%] |
|---------------------|----------------|-------------------|----------------|-------------------|----------------|
| 2 | 270.97 | 258.38 | 4.65 | 244.39 | 9.81 |
| 6 | 273.07 | 260.48 | 4.61 | 247.19 | 9.48 |
| 10 | 275.86 | 263.27 | 4.56 | 249.99 | 9.38 |

Table 8-5: Flutter speeds for the reduced box thickness for the linear deformed wing for the first torsion rigid body mode

| Angle of attack [°] | $v_{Fl,t}$ [m] | $v_{Fl,0.9t}$ [m] | $ \Delta $ [%] | $v_{Fl,0.8t}$ [m] | $ \Delta $ [%] |
|---------------------|----------------|-------------------|----------------|-------------------|----------------|
| 2 | 270.97 | 258.38 | 4.65 | 244.39 | 9.81 |
| 6 | 272.37 | 259.78 | 4.62 | 246.49 | 9.50 |
| 10 | 274.46 | 262.58 | 4.33 | 249.29 | 9.17 |

Table 8-6: Flutter speeds for the reduced box thickness for the nonlinear deformed wing for the first torsion rigid body mode

Due to the higher deformations (rotation and translation), the flutter speed of the reduced wing decreases with the thickness. This applies for the linear deformed wing as well as for the nonlinear one.

In Figure 8-2, the trend for the flutter speed is pictured and it can be noticed that for the in-plane mode the difference between the linear and the nonlinear wing is increasing with the reduction of the thickness. The linear deformed wing hereby predicts a more conservative flutter boundary. Opposing to this trend, the difference of the speeds for the torsional mode stays almost constant and the nonlinear deformed wing even has its second flutter speed a bit earlier. The percental changes for the two different flutter modes also show some differences. While for the in-plane mode the flutter boundary decreases more with increasing angle of attack, the change for the torsional flutter boundary stays almost constant. The vertical tip displacement does not change a lot with the reduced thickness (see Figure 8-3). But as mentioned before, both deformed wings have a stronger resulting gull-wing form due to the downwash (see Figure 8-4). Also, the twist differs more as a result of the torsional stiffness reduction from the thickness decrease.

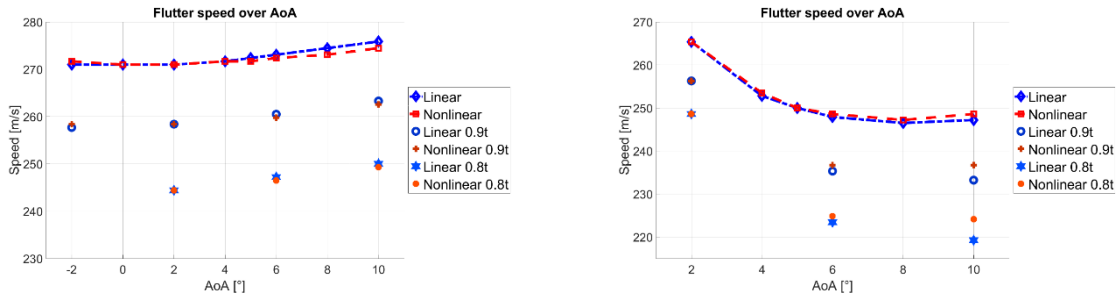


Figure 8-2: Flutter speeds of the wing with the reduced wing box thickness; for the first in-plane mode and first torsion mode

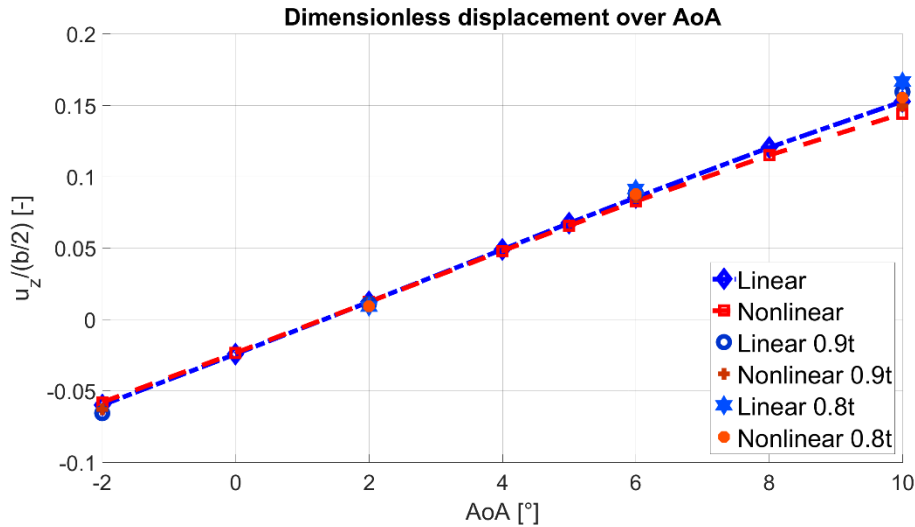


Figure 8-3: Wing tip vertical displacement for the original wing and the parametric studies

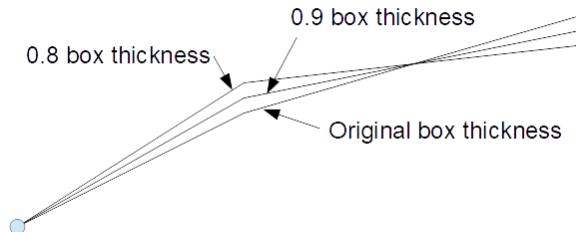


Figure 8-4: Exaggerated representation of the gull wing deformation due to mass reduction for low angles of attack

In summary, with the intention of reducing the mass of the wing by changing the structural dimension of wing box thickness, the flutter speed drops distinctly. With a resulting mass reduction of 7.3% the flutter boundary decreases between 3% and 6% for the calculated angles of attack for the linear and nonlinear deformed wing. This corresponds to a speed reduction of up to 13 m/s. With the mass reduction of 14.6% (correspondingly 0.8 wing box thickness), the flutter boundary decreases between 6% for low angles of attack and goes up to 11% for higher angles of attack. Therefore, the flutter speed reduction is up to 25 m/s.

9 Calculation of Stability Derivatives

For the estimation of the stability derivatives, the commercial program ANSYS was used. In the beginning, a mesh convergence study was carried out to find a good balance between computational cost and accuracy. It was followed by steady flow solutions for the rigid and deformed wing for several angles of attack. Here, the influence of the displacement on the quality of the coefficients C_L , C_D and C_M could be evaluated as well as the estimation of a static stability derivative ($C_{M\alpha}$).

9.1 Mesh convergence study

First, a mesh convergence study was carried out with the purpose of finding a mesh fine enough for a good prediction of stability derivatives while the calculation time is as low as possible. For that, meshes with the range of 6.5 million cells up to 80 million cells were created. The verification parameters were C_L and C_D , where the mesh was refined as far as a solution with a difference smaller than 5% being obtained. As one can see from Figure 9-1 and Figure 9-2, a convergence trend is noticeable starting from the mesh containing 30 million cells. As the calculation duration was increasing too much, the boundary conditions for a mesh with roughly 60 to 70 million cells were the preferred ones. Convergence time to a steady state solution was between 1.5 and 2 days for each case on 16 parallel processors².

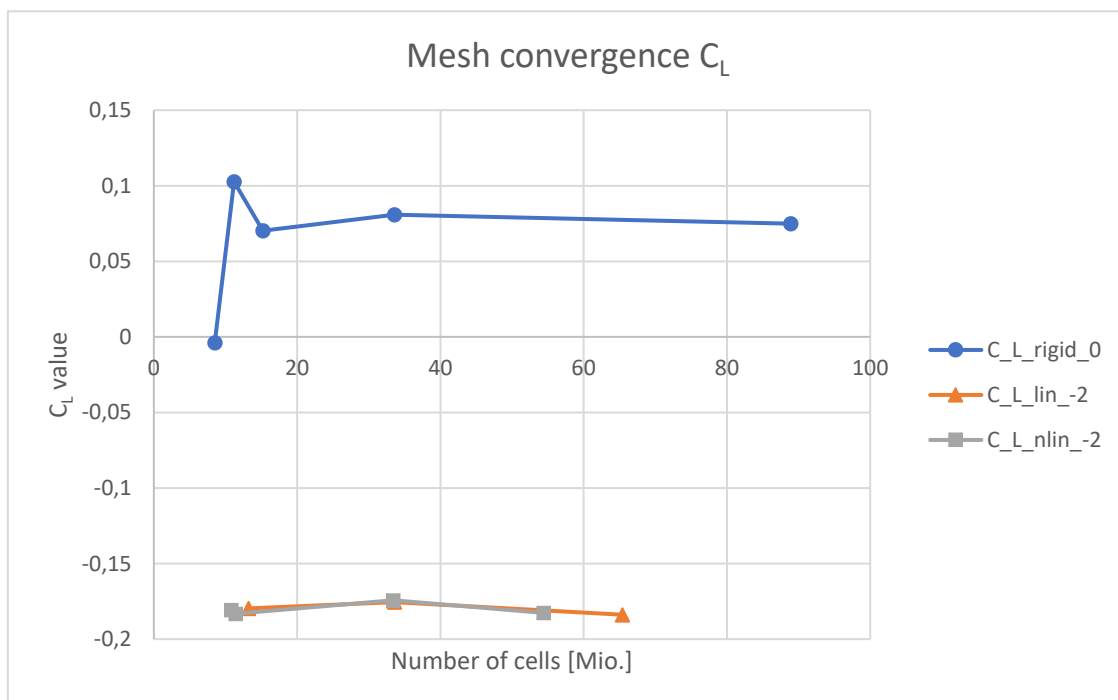


Figure 9-1: Mesh convergence study results for the lift coefficient

For the used mesh, all cases had the same refinements as following:

- Tetrahedral cells;

² Processor: Intel® Xeon® CPU X7560 2.27GHz with 4 processors (each with 8 cores); use of 16 cores in parallel to run 2 calculations with a time delay (for pre- and postprocessing)
Installed memory: 256 GB

- Face mapping on the wing;
- A bit above 600 cells span wise (edge size of 0.02m with a span of 12.6m);
- 150 cells chord wise with a refinement at the leading and trailing edge (bias factor of 30);
- Refinement at the tail for a sufficient flow depiction;
- Inflation around the wing with 30 layers and a first layer thickness of $5 * 10^{-4}m$.

The calculated y^+ , a dimensionless wall distance parameter, within Ansys and with those boundary conditions is around 200 for the wing, which for the used turbulence model (SST) is sufficient, as ANSYS has an internal correction factor (according to the help documentation). The Shear Stress Transport turbulence model is a blend of the $k - \epsilon$ and the $k - \omega$ models, which switch automatically in the CFX environment in the wake region from $k - \omega$ to $k - \epsilon$. The Reynolds number for the present case is around 30 million, with a reference length of 2.5m and a free-stream velocity of 200 m/s at sea level (corresponds to Ma 0.59)

The calculation range of interest was between -2° and 10° angle of attack, for which the wing deformation was calculated before with the MDO tool. In Figure 9-3 a), Figure 9-3 b) and Figure 9-3 e) the trend of the C_L , C_D and C_M can be seen. C_{m_α} Due to the deformation, the lift curve is flatter for the deformed wing, while the nonlinear deformed wing still has a higher and steeper lift curve, as its displacement is slightly lower.

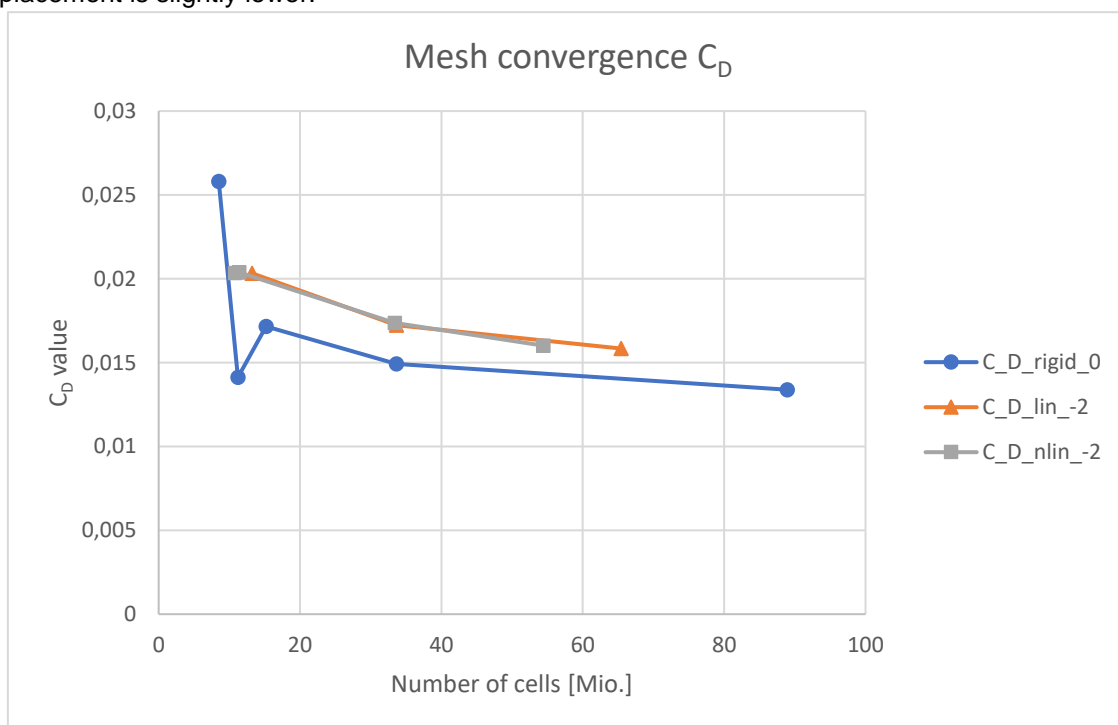


Figure 9-2: Mesh convergence study results for the drag coefficient

9.2 Results for static stability derivatives

Even though a mesh convergence study was executed in first place, a validation for the coefficients was not available as there is no comparison data from other calculations, wind tunnel or flight testing. Therefore, presented here is an estimation, where the results are compared within themselves and

trends can be observed. Nevertheless, all data should be taken carefully as experimental data could show slight differences to the data presented.

The evaluation of the lift, drag and moment coefficients took place for a range from -2° angle of attack to 10° angle of attack. However, the results for 10° for the rigid wing, are not considered, as a

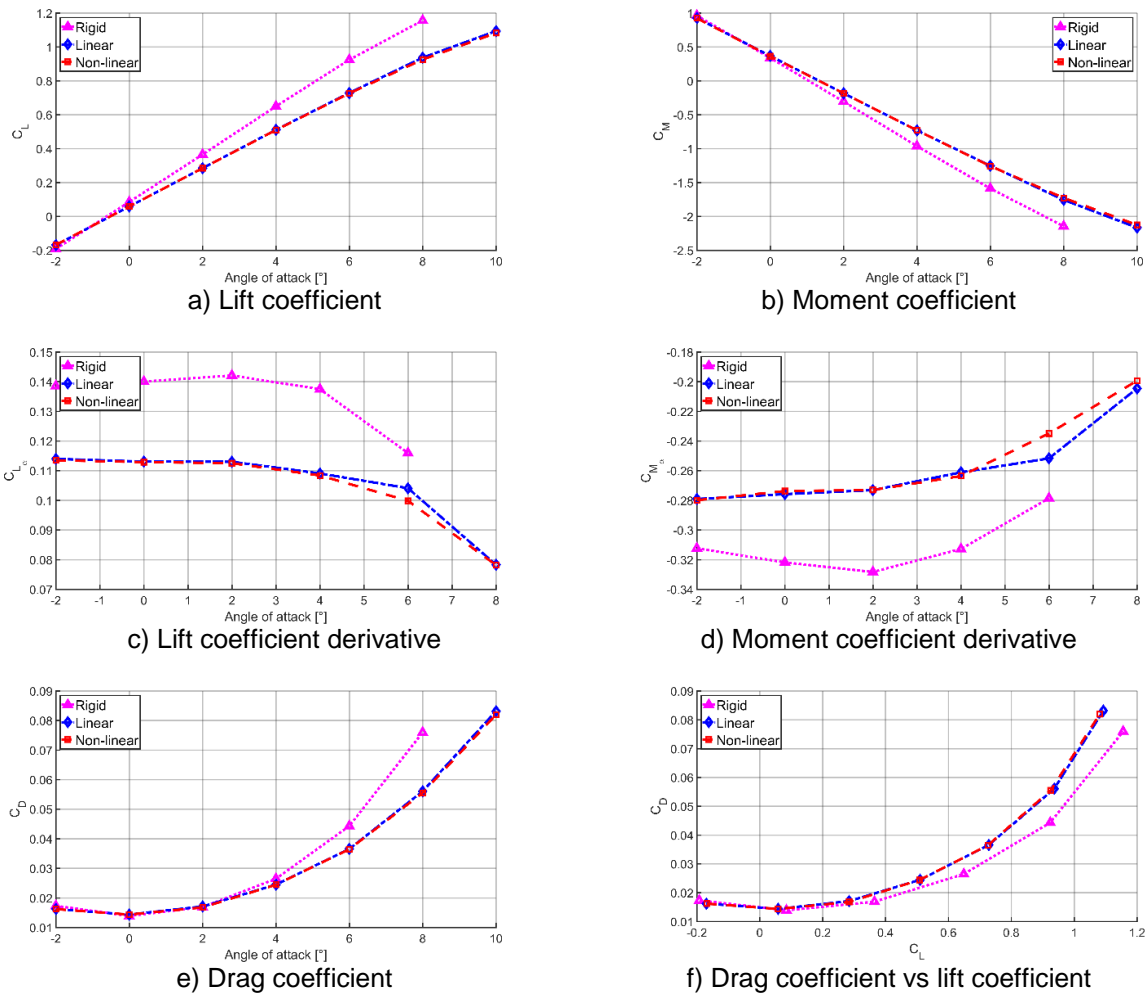


Figure 9-3: Coefficients for the coefficients of lift, moment and drag

steady solution could not be achieved. The residuals and coefficients started oscillating at some point and even with reducing the timescale, an improvement was not possible. It is assumed, that the mesh should be refined for a stable solution, but it could not be managed to execute that within the time frame of this work. For the other calculations, a steady solution could be achieved mostly within 200 steps.

The results for the coefficients can be seen in Figure 9-3 a) – f). In the calculated range between -2° and 10° angle of attack, the lift coefficient as well as the moment coefficient have an almost linear trend. It is well noticeable, that the slope of the lift and moment coefficient are lower for the deformed wings. However, the difference between the linear and nonlinear deformed wing is, likewise to the deformations and the flutter speed, relatively low. The drag coefficient is lower as well, but for the C_L vs C_D , one can notice, that the trend is higher for the rigid wing. As mentioned before, due to the distance of the calculation points, a trend can be noticed but possible abnormalities between the single points could not be caught. This would demand a higher resolution or slow dynamic calculation.

10 Conclusion and future work

This thesis aimed at the investigation of the influence of geometrical nonlinearities of structural deflections on the flight performance of a preliminarily designed wing. After a short overview of aeroelasticity and stability, the model and the computational tools, as well as their backgrounds, were introduced.

The linear and nonlinear deformations were calculated with a multidisciplinary design optimization tool and a comparison between the deformed wing took place. As measurement the vertical tip displacement was used. The result for this specific wing was a low difference between displacements of the two deformed wings. This can be explained by the low deformations, which is consistent with the literature results, where nonlinear effects have an increasing influence if the deformations are 20% of the wing semi span or higher. With the relatively low deformation of a maximum of under 16% for high angle of attack, high deformation differences weren't expected. Between linear and nonlinear deformed wing, the linear deformed one has the higher displacements for all the conditions calculated, even though they were minimal.

Ensuing, the flutter speeds for the different deformed wings and the rigid wing were calculated and compared. For low angles of attack, the rigid body starts fluttering with the first in-plane mode, while for the deformed wings it was the first torsional mode to become the flutter mode. This changed between 0° and 2° angle of attack, when the rigid body starts fluttering within the torsional mode and the deformed wings start fluttering within the in-plane mode. This also has an influence on the flutter speed itself. For low angles of attack, the rigid wing starts fluttering before the deformed ones, while for higher angles of attack, the deformed wings flutter first. Due to the higher displacements, the linear deformed wing has a flutter boundary slightly below the nonlinear deformed wing.

To see the influence of geometric properties in more detail, a short parametric study was carried out for the deformations and their influence on the flutter boundary. For that, the assumed idealized wing box was thinned out in 10% and 20% and the regarding properties were adapted to the cases. It was examined how the displacements and the flutter speeds change under this condition. The results show an almost reduced linear trend, where the geometric reduction of 10% leads to a reduction of the flutter speed of approximately 5% for the different angles of attack. For the thickness of 80% of the original box, the reduction is approximately 10%. The deformations are a bit different: at low angles of attack, the percental change is almost 10%, while at higher angles, the change is around 4%.

For stability behaviour, only a longitudinal static stability (C_{M_α}) derivative could be investigated in the scope of the work. Steady state calculations were performed for different angles of attack. The results did not show unusual values. For the coefficient of lift and moment, the trend is almost the same for all three cases (rigid, linear deformed, nonlinear deformed). The slope of the deformed wings thereby is lower than for the idealized rigid wing. Here, the nonlinear deformed wing shows even slightly lower coefficients. The static stability derivative C_{M_α} is absolute lower for the deformed wings compared with the rigid wing.

Still, there are a lot of interesting open points, which could be in the scope of further investigations. First, further parametric studies could be carried out and the magnitude of the influence on the stability derivatives could be investigated. Here, a determination of the dynamic stability behaviour (derivatives) would be interesting, as with the deformations, a more distinct response could be expected due to the high aspect ratio. However, a validation with experimental data should be considered, as for now, no such data was accessible. Especially for the CFD analysis, it would be convenient to have a comparison. Furthermore, to cover the whole flight envelope, calculations with higher speeds would be necessary. As it comes to transonic speeds, nonlinear aerodynamic effects occur, where the linear assumptions usually lead to insufficient accuracy of the results. This has to be implemented into the MDOGUI to depict also the phenomena occurring at those dynamic pressures (for instance, boundary layer separation and compressibility effects). With those models, where higher displacements would be expected, the nonlinear structural effects could be examined with even more clarity.

References

- [1] "Report of the High Level Group on Aviation Research; Flightpath 2050, Europe's Vision for Aviation on Aviation Research," Publications Office of the European Union, Luxembourg, 2011.
- [2] J. Bates, "ACI reveals that global passenger numbers to treble by 2040," in *Airport Economics 2017 Report*, 2016.
- [3] A. Abbas, J. de Vicente and E. Valero, "Aerodynamic technologies to improve aircraft performance," *Aerospace Science and Technology* 28, pp. 100-132, 2013.
- [4] J. Wolkovitch, "The joined wing: An overview," *Journal of Aircraft* 23(3), pp. 161-178, 1986.
- [5] G. Carrier, O. Atinault, S. Dequand, J.-L. Hantrais-Gercois, C. Liauzun, B. Paluch, A.-M. Rodde and C. Toussaint, "Investigation of a strut-braced wing configuration for future commercial transport, in :Proceedings of 28th International Congress of the Aeronautical Sciences (ICAS 2012)," Brisbane Australia, 2012.
- [6] I. Kroo, "Nonplanar wing concepts for increased wing efficiency". *VKI Lecture Series on Innovative Configurations and Advanced Concepts, for Future Civil Aircraft*.
- [7] R. H. Liebeck, "Design of the Blended Wing Body Subsonic Transport," *Journal of Aircraft Vol. 41, No. 1 January-February*, pp. 10-25, 2004.
- [8] S. Barbarino, O. Bilgen, R. M. Ajaj, M. I. Friswell and D. J. Inman, "A review of morphing aircraft," *Journal of Intelligent Material Systems and Structures* 22, pp. 823-877, 2011.
- [9] E. Stanewsky, "Adaptive wing and flow control technology," *Progress in Aerospace Science*, 37, pp. 583-667, 2001.
- [10] I. H. Abbott and A. E. Von Doenhoff, *Theory of wing sections, including a summary of airfoil data*, New York: Dover Publications, 1959.
- [11] AC 150/5300 - 13A, "Federal Aviation Administration," 26 2 2014. [Online]. Available: https://www.faa.gov/documentLibrary/media/Advisory_Circular/150-5300-13A-chg1-interactive-201705.pdf. [Accessed 27 09 2017].
- [12] R. F. Stengel, *Flight Dynamics*, Princeton University Press, 2004.
- [13] A. Khrabrov, K. Kolinko, O. Miatov, J. Vinogradov und A. Zhuk, „Using of Oscillatory Conning Experimental Rig for Separation of Rotary and Unsteady Aerodynamic Derivatives,“ in *18th International Congress on Instrumentation in Aerospace Simulation Facilities*, 1999.

- [14] A. C. Limache, *Aerodynamic Modeling Using Computational Fluid Dynamics and Sensitivity Equations, Dissertation*, Blacksburg, Virginia, 2000.
- [15] B.-g. Mi, H. Zhan and B.-b. Chen, "New Systematic CFD Methods to Calculate Static and Single Dynamic Stability Derivatives of Aircraft," *Mathematical Problems in Engineering*, Volume 2017, 11 pages, 2017.
- [16] B. Mialon, A. Khrabrov, A. DaRonch, L. Cavagna, M. Zhang and S. Ricci, "Benchmarking the prediction of dynamic derivatives: Wind tunnel tests, validation, acceleration methods," in *AIAA Atmospheric flight Mechanics Conference*, Toronto, Ontario, Canada, 2010.
- [17] A. DaRonch, D. Vallespin, M. Ghoreyshi and K. J. Badcock, "Evaluation of Dynamic Derivatives Using Computational Fluid Dynamics," *AIAA Journal*, Vol 50, No. 2, pp. 470-484, 2012.
- [18] C. A. Mader and J. R. R. A. Martins, "Computing Stability Derivatives and Their Gradients for Aerodynamic Shape Optimization," *AIAA Journal*, Vol. 52, No. 11, pp. 2533-2546, November 2014.
- [19] S. M. Murman, "Reduced-Frequency Approach for Calculating Dynamic Derivatives," *AIAA Journal*, Vol. 45, No.6, pp. 1161-1168, 2007.
- [20] A. DaRonch, A. J. McCracken and K. J. Badcock, "Linear Frequency Domain and Harmonic Balance Predictions of Dynamic Derivatives," *Journal of Aircraft*, Vol. 50, No. 3, pp. 694-707, 2013.
- [21] T. H. G. Megson, *Aircraft Structures for Engineering Students*, Butterworth-Heinemann, 2012.
- [22] R. L. Bisplinghoff, H. Ashley and R. L. Halfman, *Aeroelasticity*, Mineola, New York: Dover Publications, Inc., 1955.
- [23] F. W. Diederich and B. Budiansky, "Divergence of Swept Wings, National Advisory Committee for Aeronautics," 1948.
- [24] B. Von Schlippe, "The Question of Spontaneous Wing Oscillations (Determination of Critical Velocity Through Flight-Oscillation Tests)," Verlag von R. Oldenbourg, München und Berlin, 1936.
- [25] R. A. Frazer and W. J. Duncan, "The Flutter of Monoplanes, Biplanes and Tail Units (A Sequel to R. & M. 1155)," 1931.
- [26] T. Theodorson, "General Theory of Aerodynamic Instability and the mechanism of Flutter," NACA Report 496, 1935.
- [27] J. R. Wright and J. E. Cooper, *Introduction to Aircraft Aeroelasticity and Loads*, 2. Edition, Chichester: Wiley, 2015.

- [28] T. C. Corke, *Design of Aircraft*, Prentice Hall, 2003.
- [29] W. F. Phillips, *Mechanics of Flight*, Second Edition, Hoboken, New Jersey: John Wiley & Sons, Inc, 2010.
- [30] D. A. Babcock, *Aircraft Stability Derivative Estimation from Finite Element Analysis*, Master thesis, 2002.
- [31] R. C. Nelson, *Flight Stability and Automatic Control*, 1998.
- [32] G. H. Bryan, *Stability in Aviation*, London: Macmillan and Co., 1911.
- [33] N. B. Pamadi, *Performance, Stability, Dynamics, and control of Airplanes*, 2nd ed., AIAA Education Series, AIAA, Reston, VA, 2004.
- [34] D. A. Babcock und A. S. J. Arena, „Estimating Aircraft Stability Derivatives Through Finite Element Analysis,“ in *AIAA Atmospheric Flight Mechanics Conference and Exhibit*, Providence, Rhode Island, 2004.
- [35] A. C. Limache and E. M. Cliff, “Aerodynamic Sensitivity Theory for Rotary Stability Derivatives,” *Journal of Aircraft*, 2000, Vol 37, No. 4.
- [36] M. A. Park and L. L. Green, “Steady-State Computation of Constant Rotational Rate Dynamic Stability Derivatives,” in *18th Applied Aerodynamics Conference*, Denver, Colorado, 2000.
- [37] M. Ghoreyshi, A. Jirásek and R. M. Cummings, “Computational Investigation into the Use of Response Functions for Aerodynamic-Load Modeling,” *AIAA Journal*, Vol. 50, No. 6, June 2012.
- [38] F. Afonso, G. Leal, J. Vale, É. Oliveira, F. Lau and A. Suleman, “The effect of stiffness and geometric parameters on the nonlinear aeroelastic performance of high aspect ratio wings,” *Proceedings of the Institution of Mechanical Engineers, Part G: Journal of Aerospace Engineering*, Vol 231, Issue 10, pp. 1824 - 1850, 2017.
- [39] A. Suleman, F. Afonso, J. Vale, É. Oliveira and F. Lau, “Non-linear aeroelastic analysis in the time domain of high-aspect-ratio wings: Effect of chord and taper-ratio variation,” *The Aeronautical Journal*, 121, pp. 21-53, 2017.
- [40] J. Katz and A. Plotkin, *Low-speed Aerodynamics*, Cambridge University Press, 2001.
- [41] K. J. Bathe, *Finite Element Procedures in Engineering Analysis*, Prentice Hall, 1982.
- [42] W. P. Rodden and E. H. Johnson, “MSC.Nastran Version 68, Aeroelastic Analysis, User's Guide,” 2004.
- [43] E. Albano and W. P. Rodden, “A Doublet-Lattice Method for Calculating Lift Distributions on Oscillating Surfaces in Subsonic Flows,” *AIAA JOURNAL*, Vol. 7, p. 279–285, 1969.

- [44] H. J. Hassig, "An Approximate True Damping Solution of the Flutter Equation by Determinant Iteration," *Journal of Aircraft*, Vol 8, No 11, pp. 885-889, Nov. 1971.
- [45] D. J. Hodges and G. A. Pierce, Introduction to Structural Dynamics and Aeroelasticity, Press Syndicate of the University of Cambridge, 2002.
- [46] G. Leal, *Validation of a Tool for Subsonic Flutter Analysis of Straight Cantilever Wings*, Master thesis, 2013.
- [47] S. Lecheler, Numerische Strömungsberechnung, Springer Vieweg, 2014.
- [48] F. R. Menter, "Two-equation eddy-viscosity turbulence models for engineering applications," *AIAA Journal*, Vol. 32, No. 8, pp. 1598-1605, 1994.
- [49] M. J. Patil, D. H. Hodges and C. E. S. Cesnik, "Characterizing the Effects of Geometrical Nonlinearities on Aeroelastic Behavior of High-Aspect-Ratio Wings," in *Proceedings of International Forum on Aeroelasticity and Structural Dynamics, IFASD 1999*, 1999.
- [50] V. Rozov, A. Hermanutz, C. Breitsamter and M. Hornung, "Aeroelastic Analysis of a Flutter Demonstrator With a Very Flexible High-Aspect-Ratio Swept Wing," *International forum on Aeroelasticity and Structural Dynamics, IFASD 2017*, 2017.
- [51] V. Läßle, Einführung in die Festigkeitslehre, 2. Auflage, Wiesbaden: Vieweg+Teubner Verlag, 2008.
- [52] F. Afonso, J. Vale, É. Oliveira, F. Lau und A. Suleman, „A review on non-linear aeroelasticity of high aspect-ratio wings,“ *Progress in Aerospace Sciences, Volume 89*, pp. 40-57, 2017.
- [53] "MSC Nastran 2012, Quick Reference Guide," 2012.
- [54] A. DaRonch, D. Vallespin, M. Ghoreyshi and K. J. Badcock, "Evaluation of Dynamic Derivatives Using Computational Fluid Dynamics," *AIAA Journal*, Vol 50, No. 2, pp. 470-481, 2012.
- [55] M. Corporation, "FlightLoads and Dynamics User's Guide," 2006.
- [56] T. Theodorsen, "General Theory of Aerodynamic Instability and the Mechanism of Flutter," National Advisory Committee for Aeronautics, Langley Aeronautical Lab, 1949.
- [57] D. J. Hodges and G. Pierce, Introduction to Structural Dynamics and Aeroelasticity, Press Syndicate of the University of Cambridge, 2002.
- [58] C. D. Harris, "NASA Supercritical Airfoils - A Matrix of Family-Related Airfoils," Hampton, Virginia, 1990.
- [59] J. P. Giesing, T. P. Kalman and W. P. Rodden, "Subsonic Unsteady Aerodynamics for General Configurations. Part 2. Volume 1. Application of the Doublet-Lattice Method and the Method of

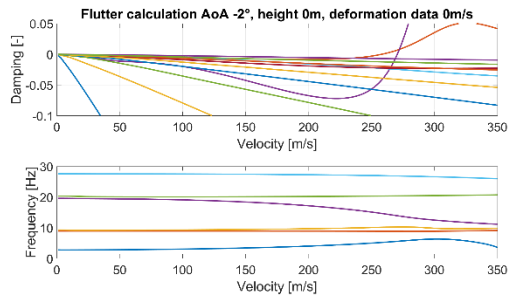
Images to Lifting-Surface/Body Interference," Technical report MDC-J0944-PT-2-VOL-1, United States Defense Technical Information Center, 1972.

Appendix

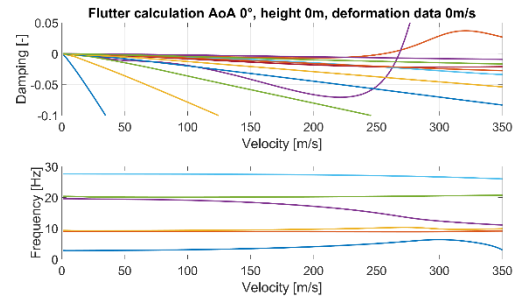
In the appendix A, the graphs for analysing the flutter behaviour can be found for the different calculations:

- At sea level with the deformed shapes at 200 m/s for an angle of attack ranging from -2° to 10° (Appendix A - 1 to Appendix A - 3).
- For a constant angle of attack of 5° and with the deformed shape data at 200 m/s, for an altitude range between -1000m and 6000m; the -1000m was for higher density reasons, whereby after 6000m no flutter occurred within the calculation range (Appendix A - 4 to Appendix A - 6).

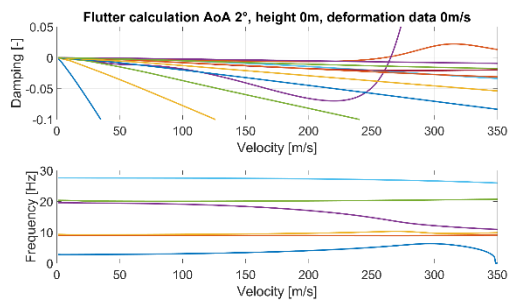
A V-g and v-f graphs



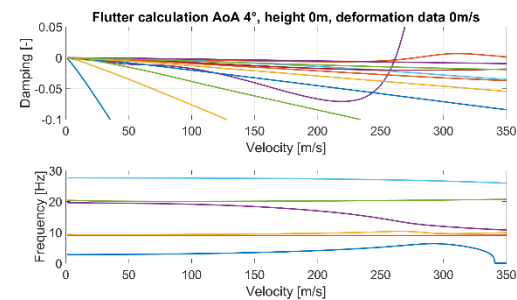
(a)



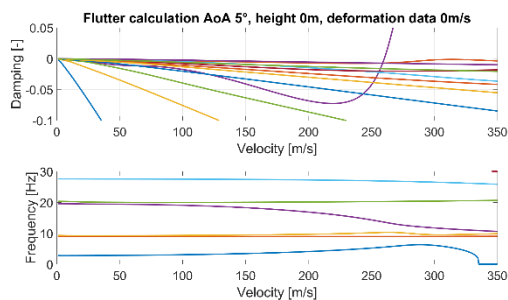
(b)



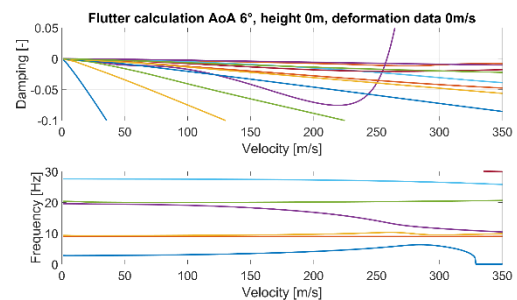
(c)



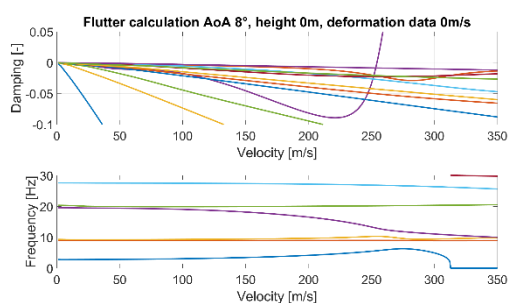
(d)



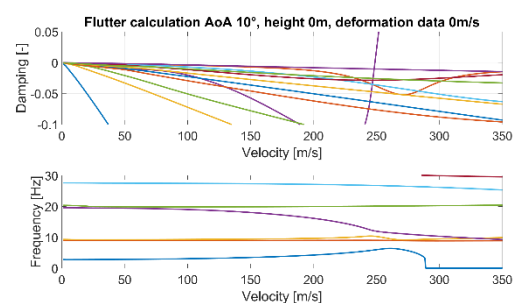
(e)



(f)

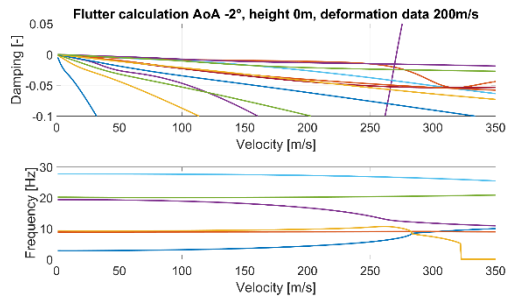


(g)

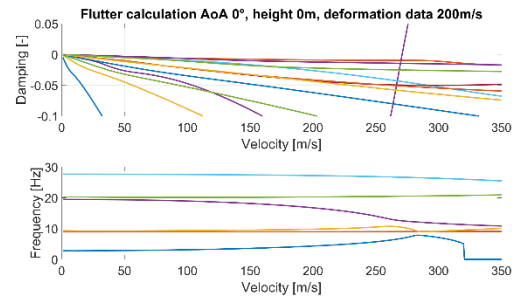


(h)

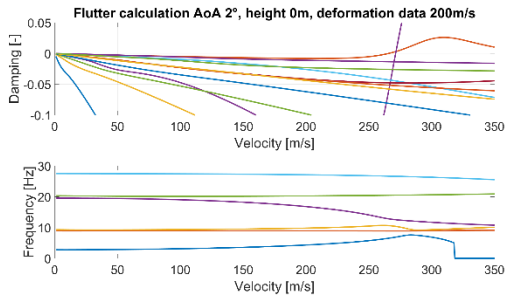
Appendix A - 1: Rigid wing flutter graphs of the changing angles of attack at sea



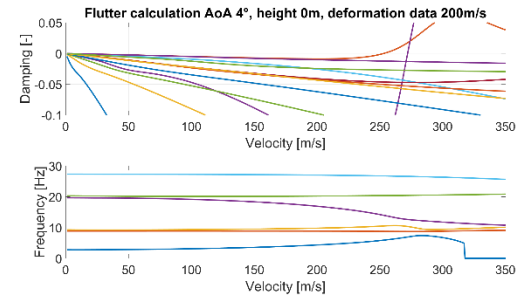
(a)



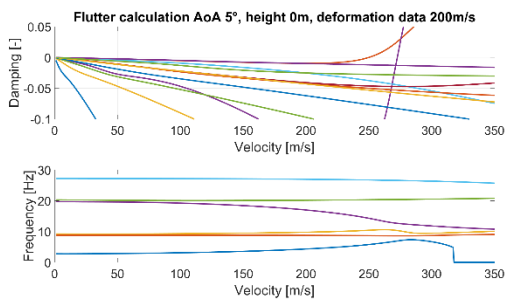
(b)



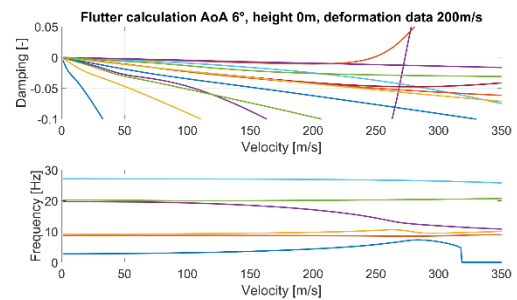
(c)



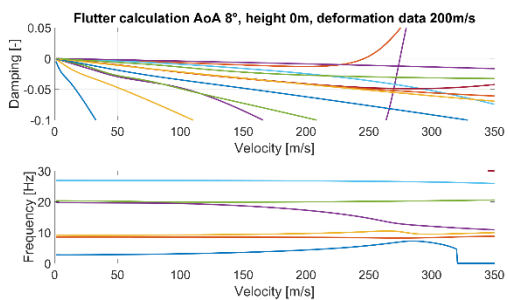
(d)



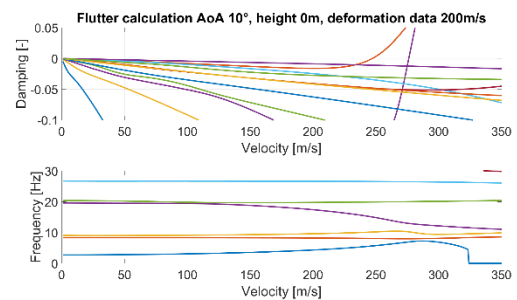
(e)



(f)

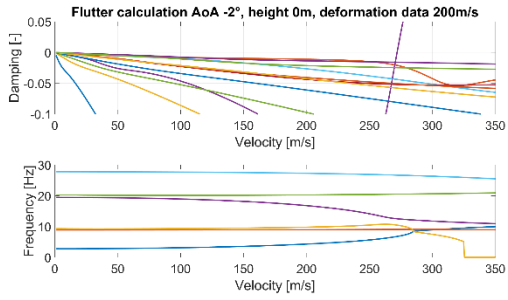


(g)

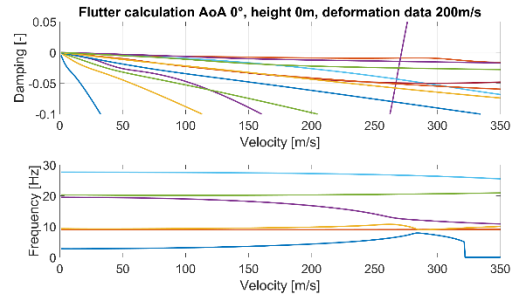


(h)

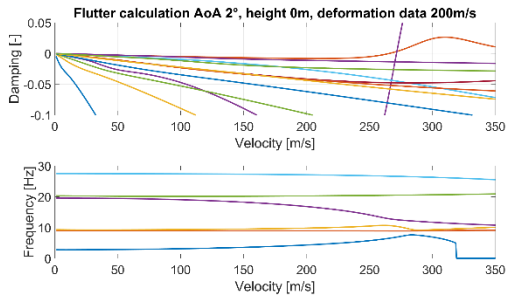
Appendix A - 2: Linear deformed wing flutter graphs of the changing angles of attack at sea level and the deformation data from 200 m/s



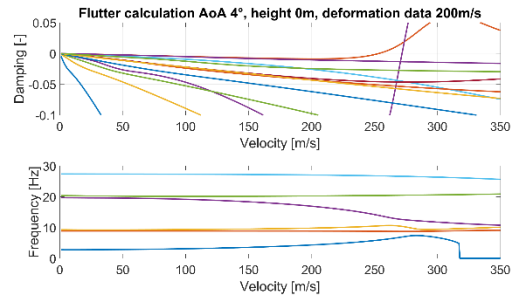
(a)



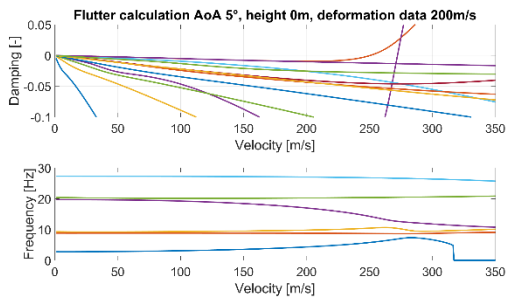
(b)



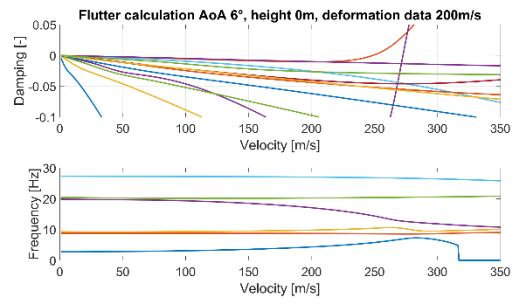
(c)



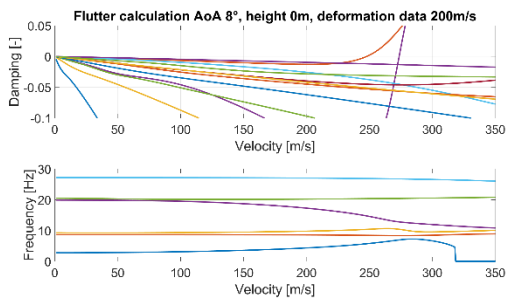
(d)



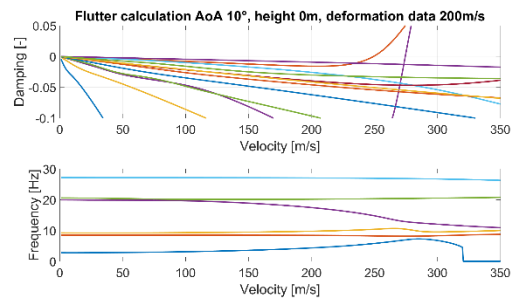
(e)



(f)

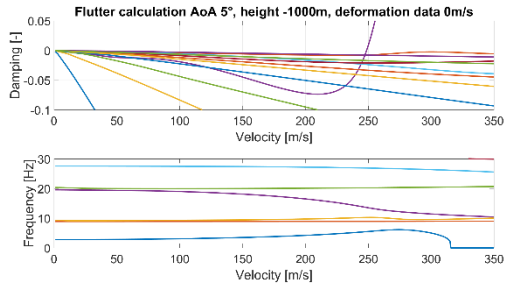


(g)

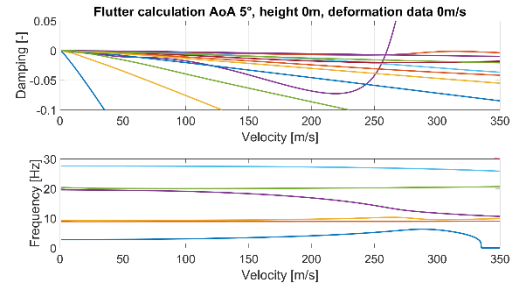


(h)

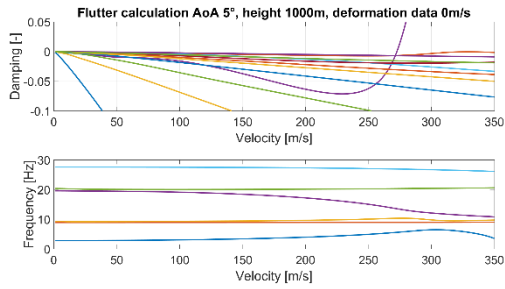
Appendix A - 3: Nonlinear deformed wing flutter graphs of the changing angles of attack at sea level and the deformation data from 200 m/s



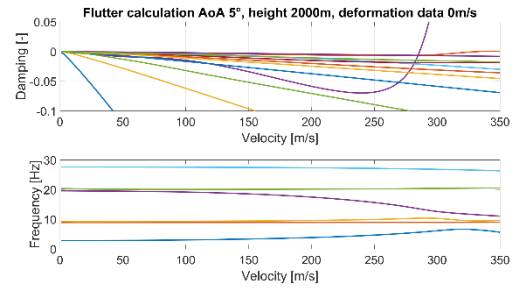
(a)



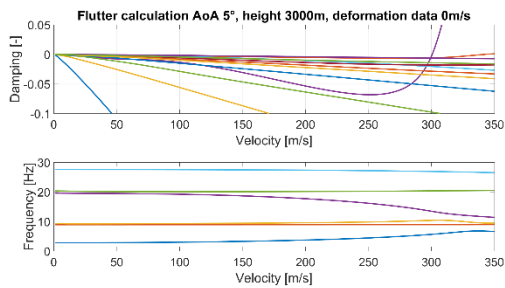
(b)



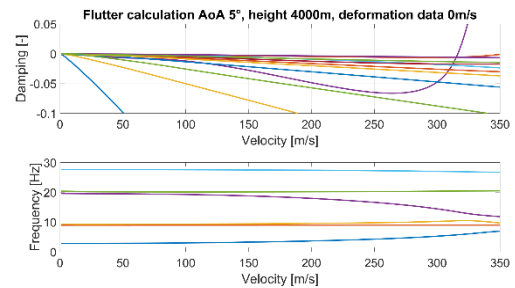
(c)



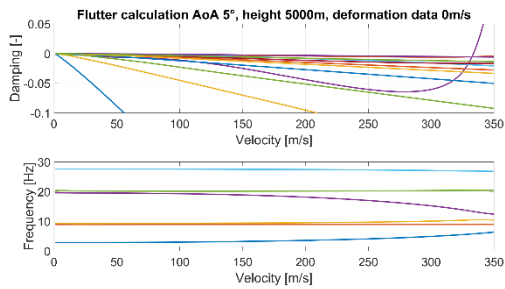
(d)



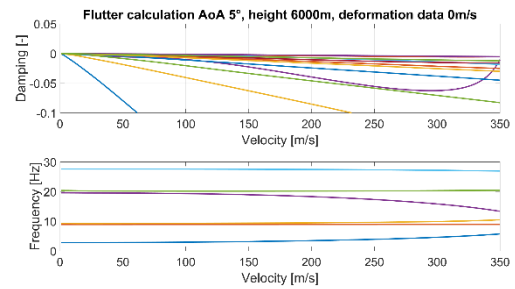
(e)



(f)

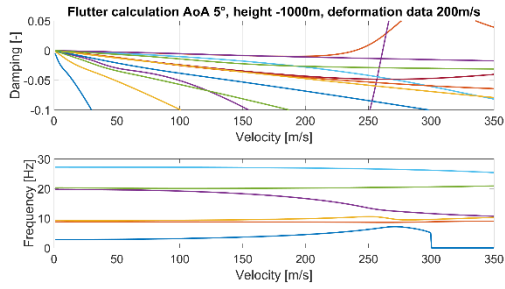


(g)

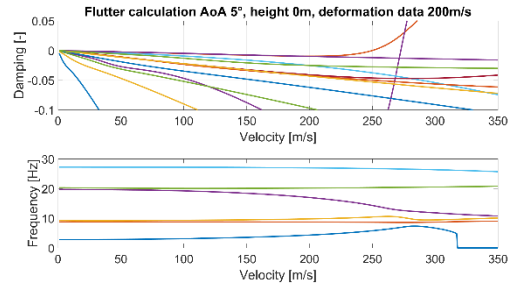


(h)

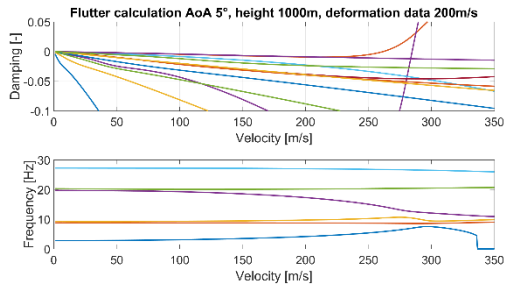
Appendix A - 4: Rigid wing flutter graphs for a constant angle of attack at different altitudes



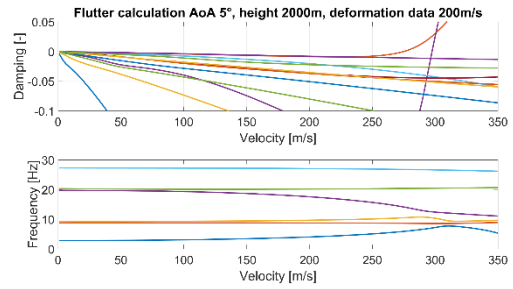
(a)



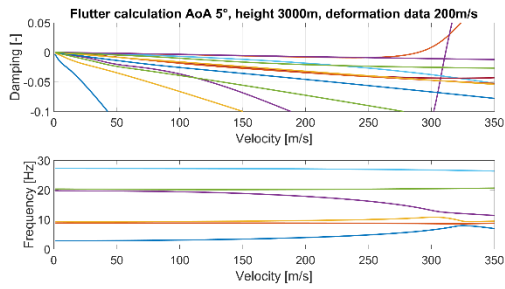
(b)



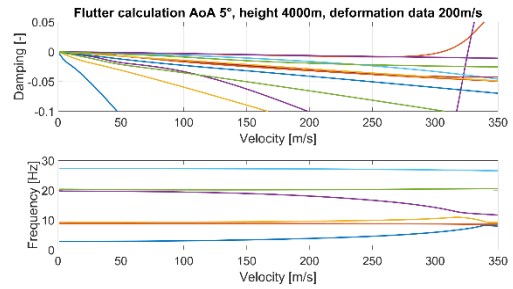
(c)



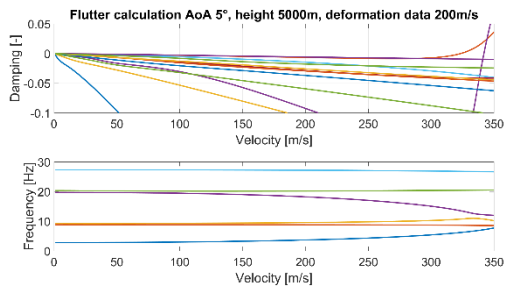
(d)



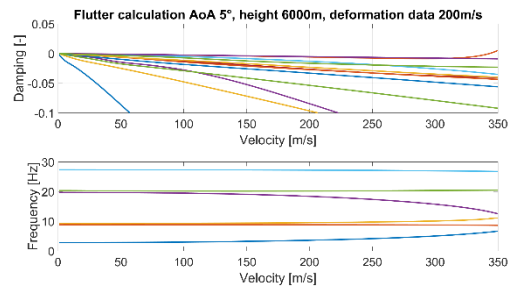
(e)



(f)

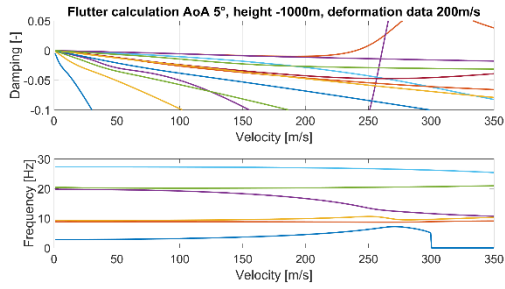


(g)

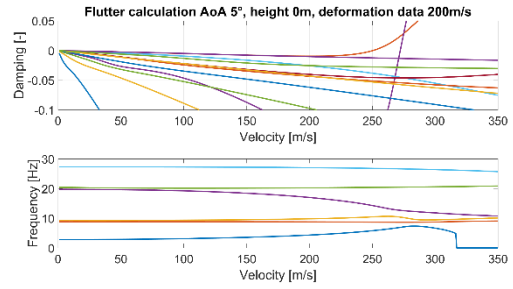


(h)

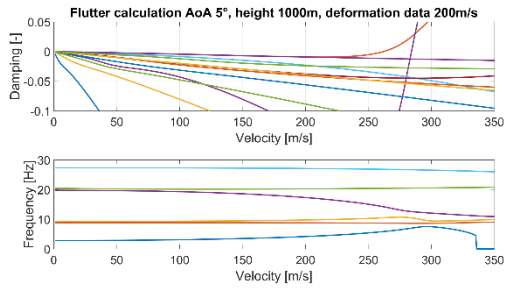
Appendix A - 5: Linear deformed wing flutter graphs for a constant angle of attack at different altitudes at the deformed state of 200 m/s



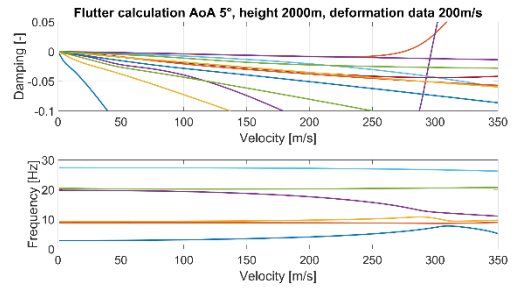
(a)



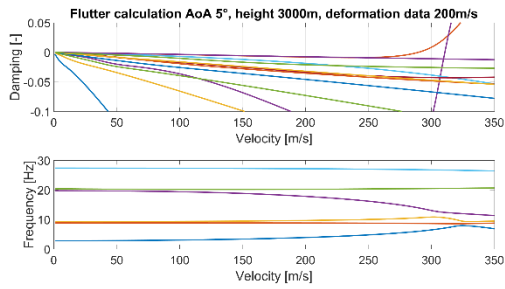
(b)



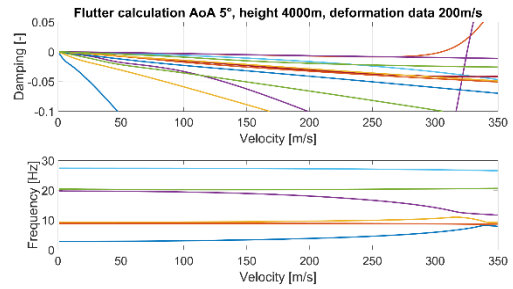
(c)



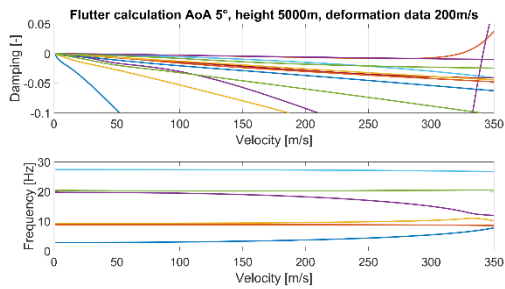
(d)



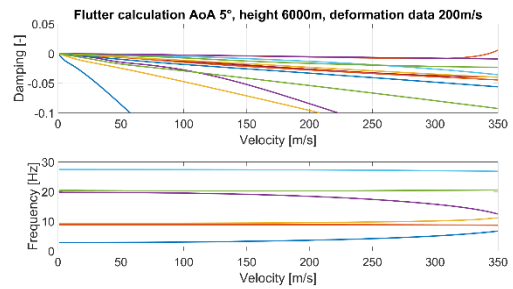
(e)



(f)



(g)



(h)

Appendix A - 6: Linear deformed wing flutter graphs for a constant angle of attack at different altitudes at the deformed state of 200 m/s